# 50-year Wind Speed Maps for Tropical Cyclone-affected Regions using Best Track data

Keeta Chapman-Smith[1], Xiaoli Guo Larsén[1], and Mark Laier Brodersen[2]

[1]Department of Wind and Energy Systems, Technical University of Denmark, Risø Campus, Roskilde, Denmark
[2]Ørsted Wind Power, Gentofte, Denmark

**Correspondence:** Keeta Chapman-Smith (kechap@dtu.dk)

**Abstract.** Accurate estimation of extreme wind speeds from tropical cyclones is a significant challenge within tropical cyclone prone regions. This study presents a method to estimate the 50-year return wind speed at heights relevant to wind turbines. The International Best Track Archive for Climate Stewardship data is combined with the Holland parametric model and the Gumbel distribution to assess extreme winds within three tropical cyclone-affected regions within the Northern Hemisphere. These regions are Taiwan, Japan, and the east coast of the United States of America. To assess the uncertainty within the results from differing input parameters, Monte Carlo simulations are used. The method aligns with previous studies through the spatial representation of wind speeds and maximum 50-year return wind speeds in Taiwan and Japan which can be attributed to the large sample size of data points located within a limited spatial area. The east coast of the United States exhibits spatial fragmentation and only partially aligns to the spatial representation of 50 year return wind speeds from previous studies, which conversely, is due to the smaller sample size and wider spatial region of which they cover. This study shows that combining International Best Track Archive for Climate Stewardship data with parametric and statistical models provides a practical approach to estimate extreme wind speeds while highlighting the need for an understanding of regional characteristics to ensure reliability of the results.

## 1 Introduction

Tropical cyclones (TCs) can be a devastating weather event, especially in coastal and offshore regions (Mortlock et al., 2018). Therefore, assessment of extreme winds is increasingly important due to the current a global expansion of offshore infrastructure, including offshore wind farms (Chen and Su, 2022).

The International Electrotechnical Commission (IEC), within standard 61400-1, provides a reference wind speed class specifically for wind turbines in TC-prone regions, known as Class T (Commission, 2019). However, it also expresses that the reference wind speed may not cover all regions prone to TCs.

There are a range of methods that have been used within previous studies to assess extreme wind speeds from TCs. For example, many have taken advantage of the International Best Track Archive for Climate Stewardship (IBTrACS) (Knapp et al., 2010; Gahtan et al., 2024). IBTrACS is a state-of-the-art dataset containing information on TC parameters such as the maximum wind speed, minimum sea level pressure, centre position, radius of maximum winds (RMW). IBTrACS is widely known and used. Of those using the IBTrACS dataset, select studies, such as (Ott, 2006; Schreck et al., 2014; Kossin, 2018) focus on general TC analysis, whereas, others such as (Bloemendaal et al., 2020b; Morin et al., 2024; Xu et al., 2024) focus on the combination of IBTrACS with other datasets to develop new synthetic datasets.

The IBTrACS dataset, however, is not without its limitations. IBTrACS does not provide the entire wind wield but rather a singular value for the maximum wind speed at each given time step. To obtain the entire wind field, parametric models, such as the Holland model (Holland, 1980), can be implemented to extrapolate a singular point into a wind field in a computationally efficient way. Parametric models are used across academic and industrial fields to investigate TCs (Arthur, 2021) and the combination of IBTrACS data with parametric models is a well used method (Ott, 2006; Fang et al., 2020; Wei et al., 2023).

In an attempt to mitigate the damage caused by extreme winds, the IEC standard defines a reference speed for each class of wind turbine. The reference speed is defined as the 10-minute wind speed average for a return period of 50 years ($U_{50}$) at turbine hub height. To align with the IEC standard, this paper focuses on these exact requirements. To calculate $U_{50}$, Generalised Extreme Value (GEV) is implemented, as previously used by Abild (1994); Larsén et al. (2015).

TC's $U_{50}$ has previously been studied, but they have rather focussed on using reanalysis data, or combining IBTrACS reanalysis data with IBTrACS (Anastasiades and McSharry, 2014), combining IBTrACS with more complex models to generate a synthetic dataset (Vickery et al., 2009; Bloemendaal et al., 2020a), or comparing extreme value analysis methods for TCs (Ott, 2006; Kong et al., 2024). Reanalysis datasets can provide useful information on TCs (Kossin, 2015) and other weather phenomena (Mavromatis, 2022; Wang et al., 2023), but they often underestimate the maximum wind speeds of TCs (Li et al., 2024), making it difficult to estimate the potential impact of TCs on offshore infrastructure (Gandoin and Garza, 2024; Liu et al., 2025). Another commonality between previous studies is the primary focus on either a single basin for winds at 10 m (Ott, 2006; Kong et al., 2024) or a limited number of specific latitude-longitude coordinates (Vickery et al., 2009; Bloemendaal et al., 2020a).

One particular study, Larsén and Ott (2022), focussed on overcoming the systematic underestimation of extreme TC wind speed within reanalysis data. The missing wind variability was filled in within the Climate Forecast System Reanalysis (CFSR) reanalysis data using a spectral correction method. The application of the spectral correction uses the $U_{50}$ estimation from Ott (2006), which in turn is based upon using the Japanese Meteorological Agency (JMA) track data (a subset of the IBTrACS dataset). This method was applied to two regions: the southwest of the northern Pacific Ocean and the western Atlantic Ocean, and, later adjusted in Imberger et al. (2024) to include two more reanalysis datasets, ERA5 [European Centre for Medium-Range Weather Forecast Reanalysis v5] and MERRA 2 [Modern-Era Retrospective analysis for Research and Applications] for where IBTrACS data is available. However, this study presents no validation through measurements.

This paper focuses on the use of the state-of-the-art IBTrACS data, updates the study of Ott (2006) which was only over the Typhoon affected southwest of the northern Pacific ocean. The regions to extended to include: the ocean around Taiwan located in the Western Pacific, the ocean around Japan also located in the Western Pacific and the east coast of the United States of America (ECUS) located in the Northern Atlantic. These have been chosen as they encompass most of the regions affected by TCs in the Northern Hemisphere and areas contain offshore wind development.

The aim of this study is, first of all, to develop a computationally efficient method to derive $U_{50}$ that can be applied across many different regions, taking advantage of the IBTrACS data. Secondly, this study investigates the applicability of the IBTrACS data in different regions for the calculation of $U_{50}$ by recognising regional TC characteristics. Thirdly, this study explicitly accounts for how uncertainties within IBTrACS propagate through to the final $U_{50}$ results. This paper is a necessary complement to Ott (2006) with its more complete use of IBTrACS data, and to Larsén and Ott (2022) and Imberger et al. (2024) due to the use of IBTrACS data.

Section 2 introduces the method developed to estimate $U_{50}$ and the accompanying uncertainty analysis using Monte Carlo simulations. Results are presented in Section 3, the uncertainty analysis is detailed in Section 4, followed by Discussions and Conclusions in Section 5 and 6, respectively. A list for abbreviation is provided in the Appendix for readability.

## 2 Method

This section will introduce and discuss the data used within the analysis and the method by which the data has been processed to obtain $U_{50}$ in three regions.

Below is a brief overview of the steps taken to calculate $U_{50}$. Each step is explained in more detail in the corresponding sections throughout the paper. Figure 1 shows the workflow of the method.

1. **Define the regions of interest**: The three regions of focus are: Taiwan, Japan, and ECUS. The exact coordinates used to define these regions are described in Section 2.2.

2. **Select relevant data**: A set of data restrictions is applied to the IBTrACS data. These restrictions are (1) the data point must fall within the region of interest, (2) the data point contain either the radius of maximum wind (RMW) or the 50 kt radius, the minimum sea-level pressure and maximum wind speed and (3) the data point is over ocean. (2) is required as they are the necessary parameter inputs to the parametric model, and (3) is required as the parametric model used to extrapolate a single data point to a wind field is only valid over ocean. The parametric model is discussed in point 4.

3. **Convert wind speeds to common averaging period**: The IBTrACS dataset is a compilation of data from agencies across the globe. Hence, the maximum wind speed is given at different averaging periods. All wind speeds are converted to a 10-minute averaging period using the method described in Harper et al. (2010). The 10-minute average was chosen as it is used as the reference speed at hub height within the IEC standard 61400-1 (Commission, 2019). Details of this conversion process are provided in Section 2.3.

4. **The Holland model**: A $0.25° \times 0.25°$ latitude-longitude grid is defined. The grid was defined to be this resolution, as a higher resolution grid requires larger computational resources, and a lower resolution could dilute key features of $U_{50}$. Once the grid is defined, the Holland model can be used. Using input parameters such as wind speed and RMW, the Holland model can extrapolate a single data point into a wind field. Following this, at each defined grid point, a corresponding wind speed value is assigned. The Holland model wind field is computed for each data point available from IBTrACS, given the data constraints. More information on the Holland model is provided in Section 2.4.

5. **Scale wind speeds to 100 m height**: The Holland model returns wind speeds at gradient height, the height at wind surface friction no longer significantly affects the wind flow. These winds are scaled down to 100 m. Any newly created data points from using the Holland model, that now fall over land, are removed. This is discussed in Section 2.5.

6. **Calculate the annual maxima**: The scaled wind fields are separated into yearly groups, and the annual maxima is calculated for each grid point. The annual maxima calculation is described in Section 2.6.

7. **Fit the Gumbel distribution**: From the annual maxima, the Gumbel distribution is fitted to estimate $U_{50}$ at each grid point. This is the final step in this method, provides a map of $U_{50}$ for each region. The process is also described in Section 2.6.

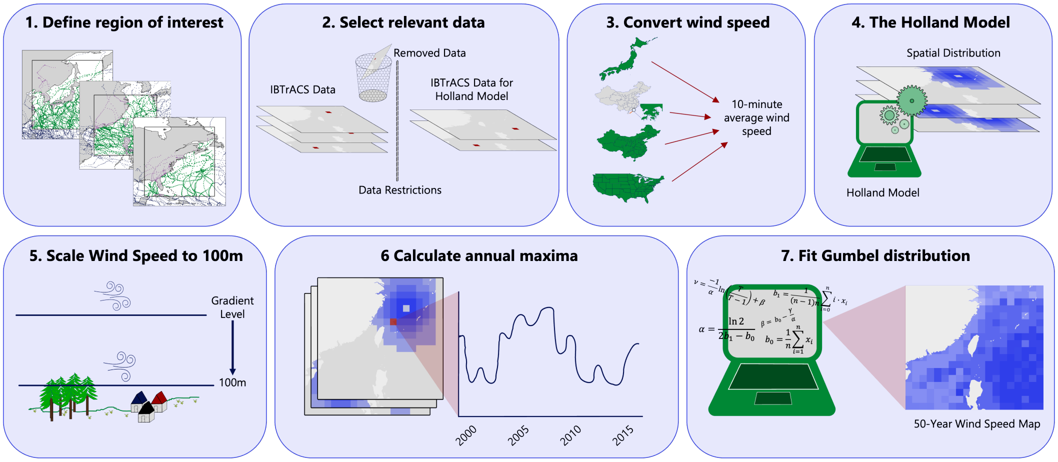

**Figure 1.** Illustration of seven-step Workflow depicting the method used to calculate $U_{50}$ at 100 m using IBTrACS.

## 2.1 Data

IBTrACS is a global tropical cyclone dataset maintained by the National Oceanic and Atmospheric Administration (NOAA). NOAA compiles post-storm records of best estimate TC parameters from multiple regional meteorological agencies, providing information such as storm position, central pressure, and maximum sustained wind speed at regular time intervals (typically every 3 hours). Every 3-hour time step, new values are provided where possible; however, a spatial realisation of the wind field (or other parameters) is not available. IBTrACS serves as a consolidated and quality-controlled reference for historical TC activity. Table 1 shows which agencies' data is available within IBTrACS, in categories of data's temporal resolution; those in bold are used in the following methods in this study. The differences between agencies pose different challenges throughout the analysis and will be detailed throughout.

Table 2 shows a comparison between the three regions: the time frame of TCs captured for this analysis, the total TCs within each region for the given time frame, the total TCs that have at least one data point with the needed parameters (maximum

**Table 1.** Wind averaging period by agency

| 1-min wind | 2-min wind | 3-min wind | 10-min wind |
|---|---|---|---|
| **US Agencies** | **China (CMA)** | India (IMD) | **Japan (JMA)** |
| | | | Australia (BoM) |
| | | | La Reunion |
| | | | Fiji (Nadi) |
| | | | New Zealand (Wellington) |
| | | | **Hong Kong (HKO)** |
| | | | South Korea (KMA) |

wind speed, RMW, minimum sea level pressure) and the number of IBTrACS data points used. The time frame of ECUS is limited by the availability of the RMW parameter and is further explained in Section 2.4. Table 3 shows a regional comparison of the grid resolution and the total number of grid points.

**Table 2.** Regional data comparison

| Region | Time frame | Total TCs | Total TCs in analysis | Total IBTrACS data points used |
|---|---|---|---|---|
| Taiwan | 1977-01-01 – 2024-12-26 | 1004 | 612 | 12447 |
| Japan | 1977-01-01 – 2024-12-26 | 819 | 608 | 13795 |
| ECUS | 2001-01-01 – 2024-12-26 | 239 | 214 | 4990 |

**Table 3.** Regional grid comparison

| Region | Grid resolution (latitude × longitude) | Total grid points |
|---|---|---|
| Taiwan | 0.25° × 0.25° | 7396 |
| Japan | 0.25° × 0.25° | 19596 |
| ECUS | 0.25° × 0.25° | 17892 |

## 2.2 Defining the “regions”

While three regions are being evaluated within this study: Taiwan, Japan and ECUS, the primary focus is the coastal areas, as this is where most offshore structures are located (e.g., Díaz and Guedes Soares (2020)). Given that TCs can be very intense systems the TC extreme winds can still have a significant impact on areas hundreds of kilometres away from the eye, and therefore, there needs to be consideration of the region chosen. The exact extent of how far damaging winds can reach is a complex subject (Weatherford and Gray, 1988; Powell and Reinhold, 2007; Chan and Chan, 2012; Knaff et al., 2021). To ensure all potential TC effects are captured, a wide area has been chosen to evaluate, as shown by Fig.s 2a, 2b, and 2c. Within these figures, a subset of IBTrACS data is shown to illustrate which IBTrACS data points are included in our calculation. A region of approximately 500 km from the most Northern, Eastern, Western and Southern points are included within the map as shown by the black square. Any data points outside of the black box have been excluded; represented as dark blue dots in the figure. The purple dots over land are also excluded from this study. The green dots represent included data points.

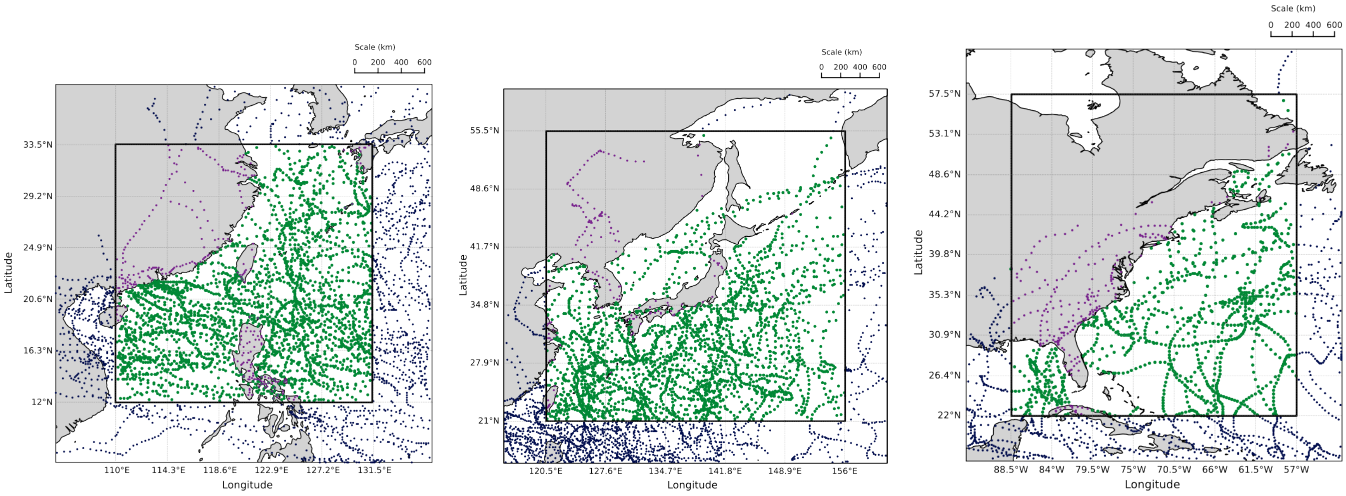

(a) (b) (c)

**Figure 2.** (a) Taiwan region. Subset: TCs in the Western Pacific, 01-01-2020 to 01-01-2025. (b) Japan region. Subset: TCs in the Western Pacific, 2020–2025. (c) ECUS region. Subset: TCs in the North Atlantic, 2021–2024. Coordinate restrictions and removed data points for each region. The inner black box represents the coordinate restrictions placed on the IBTrACS data. The dark blue dots represent excluded data points due to being outside the coordinate. The purple dots represent excluded data points due to being over land. The green dots represent data points included in the analysis. Only a subset of IBTrACS data is shown to illustrate which data is excluded.

For the ECUS region, data has been used from the pre-compiled US agencies' variables within IBTrACS. All data for the Taiwan region comes from the World Meteorological Organisation Regional Specialised Meteorological Centre in Tokyo. It is operated by the Japanese Meteorological Agency (JMA) responsible for official typhoon forecasts in the western North Pacific. The JMA dataset spans from 1951 to the present. For the Japan region, data from four agencies were combined to maximise the data availability. As previously mentioned, certain parameters are needed, and therefore, merging data from different agencies can help to fill data gaps. A hierarchy of preference was established: JMA, HKO, CMA, US. This order of preference is based on the number of available data points for the Japan region, with JMA offering the highest count of data points and the US agencies the least.

### 2.3 Wind Speed Conversion

Different agencies report the maximum wind speed of TCs using different averaging periods. To ensure consistency across datasets, all wind speeds have been standardised to a 10-minute average to align with IEC standard 61400-1. Shorter averaging periods tend to return higher wind speeds, whereas a longer averaging period results in lower wind speeds as fluctuations of turbulence are smoothed over time. Harper et al. (2010) derived algorithms to convert wind speeds measured at 10 m between different averaging periods. The conversion factors used here are provided in Table 4. The recommended procedure to convert a shorter averaging period to a lower averaging period is as follows:

The wind speed conversion factor ($CF$) for converting $x$ minute wind speed to $y$ minute wind speed, where $x < y$, is given by:

$$CF = \frac{G_{y,3600}}{G_{x,3600}}$$

where $G_{x,3600}$ is a conversion value which gives the highest $x$ second mean (gust) wind speed (for example, 600 seconds - 10 minutes) within 3600 seconds.

**Table 4.** Wind speed conversion between temporal resolutions of 1 minute to 10 minutes, and 2 minutes to 10 minutes

| | Conversion formula | At-Sea |
|---|---|---|
| 1 minute to 10 minutes | $\frac{G_{600,3600}}{G_{60,3600}}$ | $\frac{1.03}{1.11} = 0.93$ |
| 2 minutes to 10 minutes | $\frac{G_{600,3600}}{G_{120,3600}}$ | $\frac{1.03}{1.07} = 0.96$ |

### 2.4 Holland Model

The Holland model, developed by Holland (1980), is a conceptual, empirical model to extrapolate one point of data into a wind field. Figure 3 illustrates a singular data point being extrapolated to an entire wind field. The following use of the Holland model follows the method in Ott (2006). First, the $B$ parameter is calculated:

$$B = \left(\frac{V_{\text{max}}}{K_M}\right)^2 \cdot \rho \cdot e \cdot \frac{1}{(P_n - P_c)} \tag{1}$$

where $P_n$ is the minimum sea level pressure, $P_c$ is the ambient pressure, $\rho$ is air density, $V_{\text{max}}$ is the maximum wind speed at 10 m, $e$ is Euler's number, and the constant $K_m \approx 0.7$.

Using the $B$ parameter, the gradient wind speed can be calculated at distance $r$ from the TC centre:

$$V_g = \sqrt{\frac{P_n - P_c}{\rho} \cdot B \cdot \left(\frac{R_0}{r}\right)^B} \cdot \exp\left(-\frac{\left(\frac{R_0}{r}\right)^B}{2}\right) \tag{2}$$

where $R_0$ is the RMW.

The RMW parameter is collected only by US agencies. Prior to 2001, the data availability of this parameter was limited to at most seven data points per year, restricting the use of the US data to be from 2001 onwards.

The JMA dataset does not provide the RMW, but the 50 kt radius is provided. Specifically, the longest and shortest radii for 50 kt winds are reported, from which the RMW can be estimated. This data is available from 1977 onward. The JMA dataset only covers the Western North Pacific, and the 50 kt radii is not available for the ECUS region.

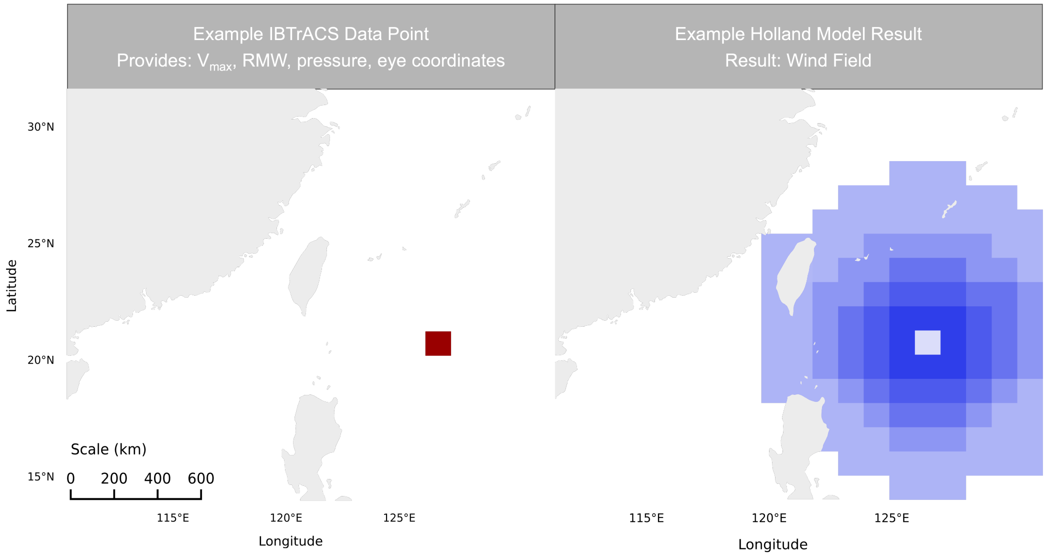

**Figure 3.** Illustration depicting an example data point from the IBTrACS dataset and the wind field result from using the parameters from the data point as an input into the Holland model.

## 2.5 Height scaling for wind

The Holland model outputs wind speed at gradient level (Holland, 1980); the height at which surface friction no longer significantly affects the wind flow. Therefore, the wind speed needs to be scaled to a height that is of use. For this paper, the wind speed has been scaled to 100 m. Franklin et al. (2003) suggests that, for TCs, the layer below the broad maximum wind speed of 500 m, approximately follows the logarithm of the altitude. To scale the wind, firstly, the geostrophic drag law is solved for the friction velocity (Rossby and Montgomery, 1935; Blackadar and Tennekes, 1968):

$$\mathrm{G} = \frac{u_*}{\kappa}\sqrt{\left(\ln\left(\frac{u_*}{f_{\mathrm{col}}\cdot z_0}\right)-A\right)^2+C^2} \tag{3}$$

where $u_*$ is the friction velocity, $G$ is the geostrophic wind, $\kappa$ is the con Kármán constant, $f_{\mathrm{col}}$ is the Coriolis parameter, $z_0$ is the surface correction parameter and $A$ and $C$ are constants defined by the neutral conditions. The constants are set as $A = 1.8$ and $C = 4.5$. Using the friction velocity, the wind speed is scaled to a different height using the logarithmic wind law:

$$u(z) = \frac{u_*}{\kappa}\ln\frac{z}{z_0} \tag{4}$$

where $z$ is the target height. Combining the geostrophic wind law with the logarithmic profile of the wind is a well-established method and already implemented into systems such as Wind Atlas Analysis and Application Program (WAsP) (Troen and Petersen, 1989).

The wind speeds were originally scaled to 10 m for comparison against the IBTrACS dataset. The approach was performed for varying surface correction parameters for each region. The optimal surface correction parameter was selected by evaluating, on average, how well the scaled wind speeds match the 10 m IBTrACS data. The adjusted values for the surface correction parameter identified are $5e^{-6}$ m, $9e^{-6}$ m and $1e^{-5}$ m for the Taiwan, Japan and ECUS regions, respectively. Note that while the roughness length would usually be used, here a surface correction parameter is used in its place. The rationale for this approach is discussed in detail in Appendix A.

The commonly accepted deep ocean surface roughness value is 0.2 mm (He et al., 2021). However, Ott (2006) shows that the eyewall profile follows the logarithm of the altitude using a surface roughness of 0.07 mm.

To scale to 100 m, the same method was performed using the adjusted roughness length.

### 2.6 The Gumbel Distribution

For each individual grid point and for each year, the maximum wind speed at 100 m is obtained following Section 2.4 and 2.5. Using the annual maxima, the Gumbel distribution estimates $U_{50}$. This method follows the approach described in (Abild, 1994; Larsén et al., 2015) in which $\mathbf{X}_m$ is the ascending sorted annual maxima (for each grid point), with $n$ samples.

The sample mean is computed:

$$b_0 = \frac{1}{n}\sum_{i=1}^{n} X_{m,i} \tag{5}$$

and the weighted mean

$$b_1 = \frac{1}{(n-1)n}\sum_{i=1}^{n}(i-1)\cdot X_{m,i} \tag{6}$$

The Gumbel distribution parameters $\alpha$ and $\beta$ can be calculated such that:

$$\alpha = \frac{\ln 2}{2b_1 - b_0} \text{ and } \beta = b_0 - \frac{\gamma}{\alpha} \tag{7}$$

where $\gamma$ is Euler's constant = 0.57721. The wind speed for the return period $T$ is

$$U_T = -\frac{1}{\alpha}\ln\left(\ln\left(\frac{T}{T-1}\right)\right) + \beta \tag{8}$$

and the standard deviation associated with the wind speed for the return period $T$ is

$$\sigma_T = \frac{\pi}{\alpha\sqrt{6n}}\sqrt{1 + 1.14\,k_T + 1.1\,k_T^2}\,. \tag{9}$$

where $k_T = \frac{\sqrt{6}}{\pi}\left(-\ln\left(\ln\left(\frac{T_{\text{return}}}{T_{\text{return}}-1}\right)\right) - 0.577\right)$

Using the yearly maximum for the Gumbel fit can result in the discarding of other large storms that occur in the same active year. This, in turn, could lead to the tail retaining less information than other approaches. Since $U_{50}$ is derived in the Gumbel distribution by extrapolating the fitted tail to an exceedance probability, the estimate could carry additional uncertainty. A peak-over-threshold approach using the Generalised Pareto distribution was tested, but the grid resolution produced too few exceedances per point. This lead to unstable and often negative shape parameters. The Gumbel distribution remains a standard choice but for this procedure, the resulting $U_{50}$ represents the wind level associated with exceedance of the yearly maximum, rather than the full set of extreme storms that may occur within a year.

## 3 Results

The results of calculating $U_{50}$ are presented in three regions: Taiwan, Japan and ECUS regions are shown here. Each region will be discussed individually.

### 3.1 Taiwan

In Figure 4a, $U_{50}$ at 100 m is presented for the Taiwan region. The region expands from latitude $12° N$ to $33.5° N$ and longitude $110° E$ to $131.5° E$. Taiwan is located in the centre of the figure, with the Philippines to the south and mainland China to the west.

The highest values of $U_{50}$ are observed east of longitude $120° E$, corresponding to areas east of Taiwan and the Philippines. In contrast, in the west of Taiwan and the Philippines, the wind speed is slower by approximately 10 - 20 m $s^{-1}$. The majority of TCs forming in the Western Pacific form to the south-east of Taiwan (Guo et al., 2025), where they can intensify before weakening as they approach or move over land (Park et al., 2013). Therefore, it is expected to see the highest winds south-east of Taiwan, before reaching land. The spatial distribution of the wind field looks somewhat consistent with previous studies based on IBTrACS data, such as Ott (2006); Kong et al. (2024). To compare with the results of Ott (2006); Kong et al. (2024), $U_{50}$ at 10 m is also provided here (Fig. 4d). The maximum value of $U_{50}$ at 10 m in this area is 72.7 m $s^{-1}$, which is 72 m $s^{-1}$ in Ott (2006) and 70.4 m $s^{-1}$ in Kong et al. (2024). Figure 4d here also includes more detailed spatial variability of $U_{50}$ at 10 m than Ott (2006) and Kong et al. (2024) due to their larger spatial grid spacing of 1° x 1°. It should be noted that the spatial distribution of Fig 4a and 4d is very similar and the 10 m results simply return smaller values. The detailed spatial distribution of $U_{50}$ at 100 m in this study is similar to the results in Larsén and Ott (2022) (their Figure 7a), which was based on the CFSR reanalysis data with grid spacing of about 40 km, where the values of $U_{50}$ were corrected to an equivalent temporal resolution of 10 min. While Imberger et al. (2024) presents results at 50 m and 150 m using CFSR, MERRA 2, and ERA5, the resultant dataset from the project has also been made available. Examining the 100 m results, the spatial distribution appears most similar to the CFSR output, with the peak located to the east of the Philippines. Whereas, for the ERA5 and MERRA 2 results, the peak is located further north. The maximum $U_{50}$ at 100 m in this analysis is 84.3 m $s^{-1}$, which is closest to the ERA5 estimate of $U_{50}$ of 86.7 m $s^{-1}$.

The 95% confidence interval calculated using Eq. 9 in connection with the use of Gumbel distribution is shown in Fig. 4b. It widens in areas where $U_{50}$ increases, peaking at approximately 15 m $s^{-1}$, and it narrows to approximately 2 m $s^{-1}$ at the smallest. In this context, the 95% confidence interval reflects the variability associated with the fitted Gumbel distribution. It does not represent the uncertainty of all input parameters. Uncertainties relating to the entire process are discussed in Section 4. Given that the Holland model is applied to every IBTrACS data point that fits the criteria, all grid points have the same number of data points which are listed in Table 2. To illustrate which areas in each region contain the highest wind speeds Figure 4c has bee developed. It shows the number of data points above 19 m $s^{-1}$ from the Holland model at each grid point. NOAA defines a tropical storm when the 1-minute average winds reach 34 kt at 10 m. By converting 34 kt to m $s^{-1}$, a 10-minute average and scaling the wind speed height to 100 m, the threshold becomes 19 m s$^{-1}$. These methods are all described in Section 2. The same reasoning holds true in Sections 3.2 and 3.3.

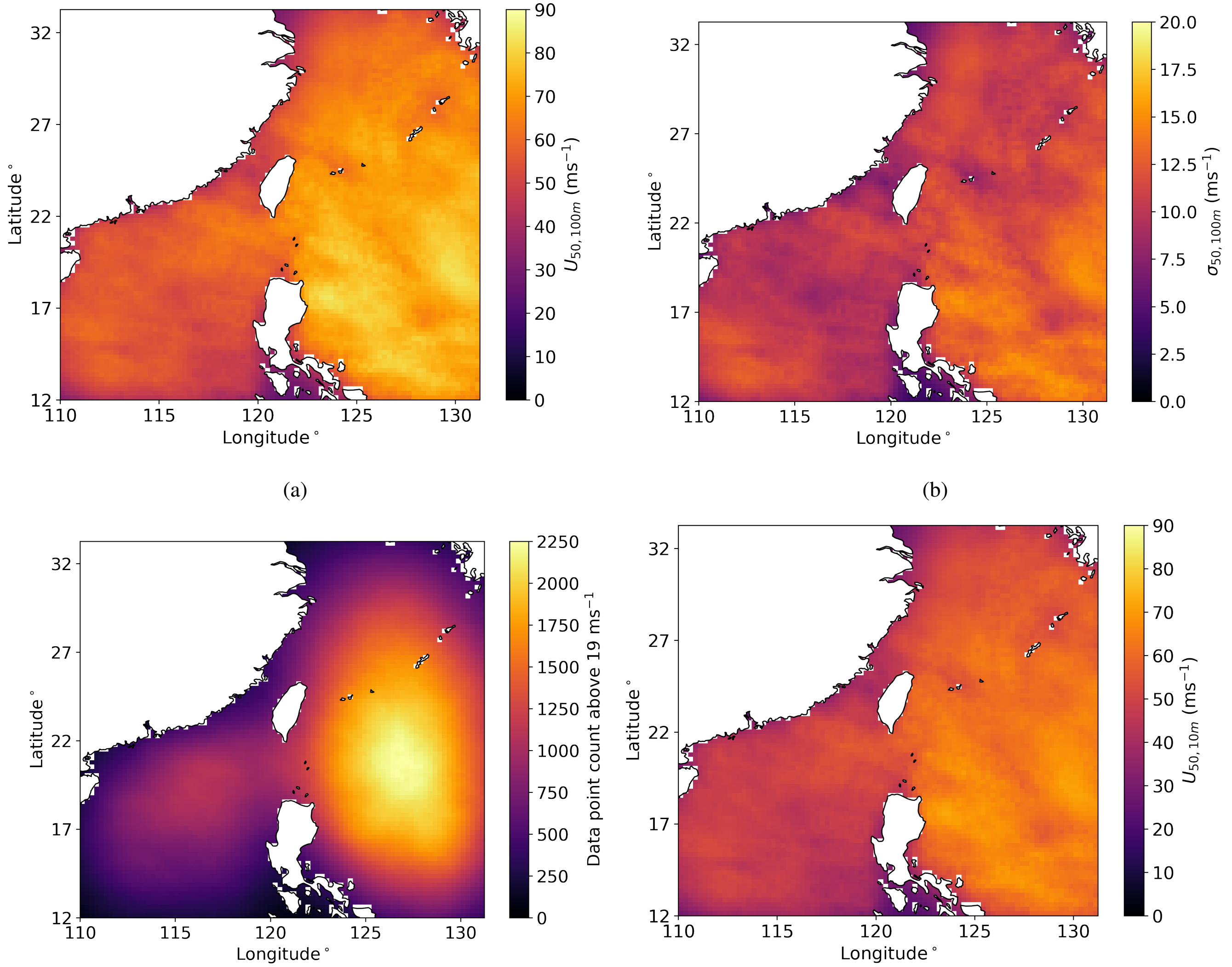

(a) (b)

(c) (d)

**Figure 4.** Results for Taiwan. (a): $U_{50}$ at 100 m. (b): The 95% confidence interval from the Gumbel distribution calculated using 1.96 $\sigma_{50}$. (c): The number of data points from the Holland model calculation that are equal to or above 19 m s$^{-1}$. (d): $U_{50}$ at 10 m.

### 3.2 Japan

In Figure 5a, $U_{50}$ at 100 m is presented for the Japan region. The region expands from latitude 21°$N$ to 55.5°$N$ and longitude 120.6°$E$ to 156°$E$. Japan is located in the centre of the figure, with South Korea, North Korea, Russia and China located to the west. In this region, the genesis of TCs typically occurs at lower latitudes, and they move in a north-west direction. The Coriolis force turns the TCs further north, and once it has reached mid-latitudes, the TC turns eastward due to westerlies in addition to the Coriolis force (Cao et al., 2025). As they move north, the sea water temperature typically becomes cooler and the TC weakens (Fei et al., 2020), hence the higher $U_{50}$ values occurring at latitudes lower than $36^\circ N$ while the TC still holds intensity. In Figure 5c, showing the number of values each grid point has above 19 m s$^{-1}$, there are far fewer data points above $36^\circ N$ degrees latitude in comparison to below $36^\circ N$ degrees latitude, and above $46^\circ N$ degrees latitude there are few to no data points giving explanation as to why wind speeds approach 0 m s$^{-1}$ in this region. However, this does not mean that the extreme wind speed in these areas is negligible, as other weather processes can take place, but this study solely focuses on tropical cyclone extreme wind speed. This clearly demonstrates the uncertainty associated with too few data samples.

The southern coastline of Japan is the most exposed, though both the southwestern and southeastern coastlines still experience elevated wind speeds due to TCs. As in the Taiwan region, the 95% confidence interval increases with wind speed, reaching its highest values in areas where there is substantial and strong TC activity.

The spatial distribution as well as the magnitude of $U_{50}$ at 100 m in Fig. 5a is quite similar to that in Larsén and Ott (2022) (their Fig. 7a) for the overlapping area, including the patchy patterns. Such levels of detail are absent in Ott (2006) and Kong et al. (2024) due to the coarser spatial resolution. The results presented here differ spatially from Imberger et al. (2024). In Imberger et al. (2024), peak wind speeds occur primarily below $35^\circ N$ and up to $140^\circ E$, with a north-eastward trailing feature. In contrast, this analysis shows a less pronounced decrease beyond $140^\circ E$ and does not capture this north-eastward feature. This could be due to the difference in sample size at high latitudes, as the dataset used in Imberger et al. (2024) does not exhibit the same reduction in data availability with increasing latitude. The maximum $U_{50}$ in this study is lower than all values used in Imberger et al. (2024), however, the ERA5 and MERRA 2 maxima are shifted further north into the Japan region, where as the CFSR results are more consistent with those presented here, aside from a single pronounced peak in the Imberger et al. (2024) analysis.

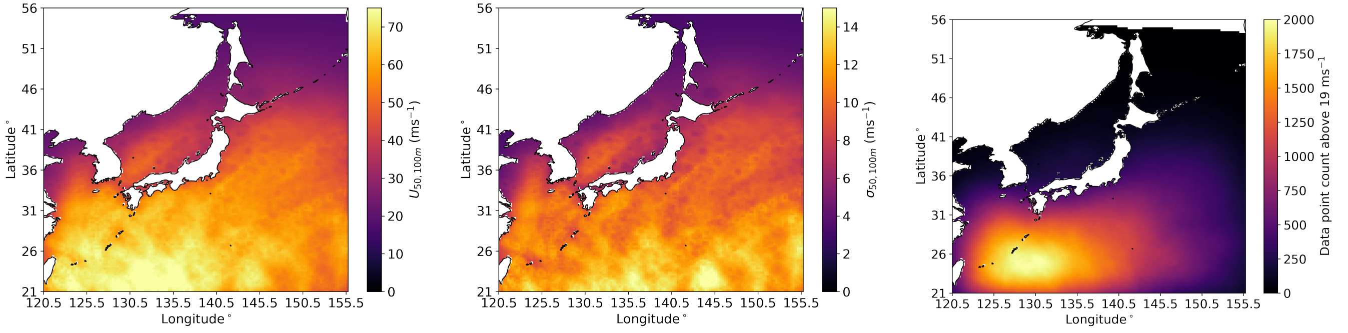

(a) (b) (c)

**Figure 5.** Results for Japan. (a): $U_{50}$ at 100 m. (b) The 95% confidence interval from the Gumbel Distribution calculated using 1.96 $\sigma_{50}$. (c): The number of data points from the Holland model calculation that are equal to or above 19 m s$^{-1}$.

### 3.3 East Coast of the United States

In Figure 6a, $U_{50}$ at 100 m is presented for the ECUS region. The region expands from latitude 22$^\circ N$ to 57.5$^\circ N$ and longitude 88.5$^\circ W$ to 57$^\circ W$. The east coast of the United States of America is shown, along with the top of the Caribbean in the south.

The results from the ECUS region deviate from expectations. At a granular scale, the eyewall of the TC is evident as it traverses over the region, and the $U_{50}$ field exhibits a fragmented structure, which will be discussed in Section 5. On a macro scale, the spatial distribution of $U_{50}$ maxima and minima is unexpected. The highest wind speeds were anticipated to occur consistently within the lower half of the region. This distribution was expected due to the positive correlation between latitude and RMW (Kimball and Mulekar, 2004; Vickery and Wadhera, 2008; Pérez-Alarcón et al., 2021) and TCs within the Gulf of Mexico, on average, have a smaller RMW than those in the Atlantic (Vickery and Wadhera, 2008). The intensity of a TC is inversely related to the RMW (Kimball and Mulekar, 2004; Chavas and Knaff, 2022), meaning, on average, storms with smaller RMW tend to have stronger winds than TCs with large RMW.

The results here show, that while the highest return level is 74.9 m s$^{-1}$ at 26.75$^\circ N$ degrees latitude and 64.75$^\circ W$ degrees longitude, the latitude further north also exhibits return levels which are nearly as high. The wind speeds between latitudes 33$^\circ N$ and 40$^\circ N$ and longitudes 64.5$^\circ W$ and 59.5$^\circ W$ are noted as rather high.

The 95$\%$ confidence intervals follow the same pattern as in the previous cases: regions with higher wind speeds correspond to a widening confidence interval. Furthermore, the confidence interval structure also follows the same structure as $U_{50}$.

The study of Larsén and Ott (2022), reflecting the reanalysis CFSR wind field, does suggest a stronger $U_{50,100m}$ band south of 30°$N$, between about (30°$N$, 75°$W$) and (22°$N$, 65°$W$), with the highest value of about 73 m s$^{-1}$. Due to the Coriolis force and westerlies, this strong $U_{50,100m}$ band turns north-east (their Fig. 7c). Compared to Larsén and Ott (2022), Fig. 6a here captured the second, relatively weaker extreme wind band north of 30 °$N$, and did not capture the full picture of the first, stronger extreme wind band. We argue that it is, on one side, caused by the few IBTrACS tracks in this region (see Fig. 6c), and on the other side, related to the application of the Holland model. The detailed discussion is provided in Section 5. The hotspot in the Caribbean is both present in the current study and in Larsén and Ott (2022). Imberger et al. (2024) identifies a Caribbean hotspot across all three datasets. In addition, the CFSR results show a separate, lower-latitude hotspot in the Atlantic Ocean, which is not evident in the ERA5 or MERRA 2 outputs which this analysis is more inline with. The CFSR and MERRA 2 datasets otherwise place their primary peaks above 35°N. The maximum wind speed in this analysis (74.9 m s$^{-1}$) is closest in magnitude to the CFSR value of 72.0 m s$^{-1}$, although the locations of these maxima differ substantially.

## 4 Uncertainty Analysis

As outlined in Section 2, there are several input parameters into the Holland model and the Gumbel distribution, which could introduce uncertainty into the estimation of $U_{50}$. Given the number of contributing variables, a Monte Carlo (Metropolis and Ulam, 1949) approach was used to propagate uncertainty throughout the method. The parameters considered include wind speed, centre position, RMW, pressure, the $B$ parameter, and scaled wind speed. Monte Carlo simulations are a common

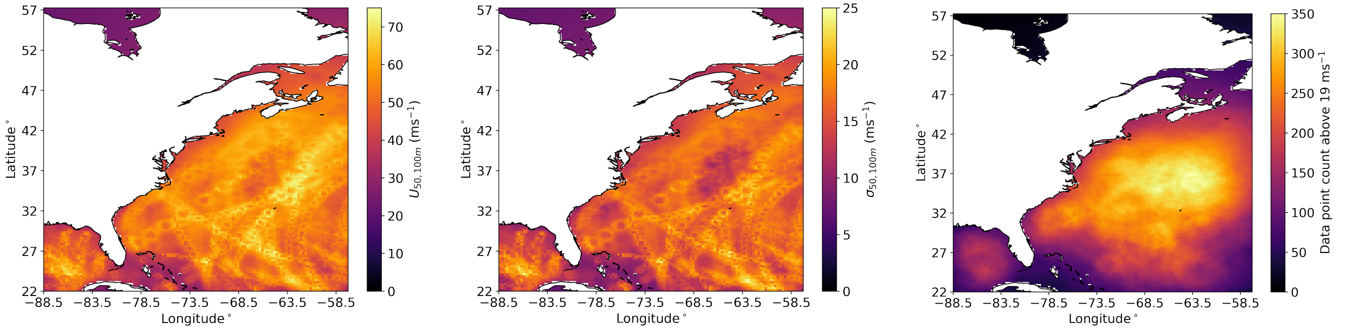

(a) (b) (c)

**Figure 6.** Results for ECUS. (a): $U_{50}$ at 100 m. (b): The 95% confidence interval from the Gumbel Distribution calculated using 1.96 $\sigma_{50}$. (c): The number of data points from the Holland model calculation that are equal to or above 19 m s$^{-1}$.

method to estimate uncertainty within the wind energy sector, as shown by Ishihara and Yamaguchi (2015); Yasui et al. (2002); Hu et al. (2023)

Most parameters within the uncertainty analysis are sourced from the IBTrACS dataset, and while data from many agencies are consolidated, the associated errors are not, making the quantification of uncertainty challenging. IBTrACS is typically used as a reference dataset for validation purposes and does not consistently report uncertainty estimates for all variables. Therefore, bespoke methods to quantify each parameter's uncertainty have been used. Some parameters have a uniform range defined, others require comparison of values from various agencies for a standard deviation to be calculated, and one requires error propagation.

The uncertainty associated with the sampling rate of IBTrACS is not quantified in this section. The dataset provides 3-hourly observations, and no interpolation to a finer resolution was performed to avoid introducing additional uncertainty. The aim is to evaluate the method using the raw IBTrACS data. A second source of uncertainty that has not been extensively evaluated is the climatological variability of the underlying dataset. An attempt was made to quantify this by splitting each regional dataset into two equal halves and fitting the Gumbel distribution independently to each half. The difference between the two half-period estimates was tested for statistical significance by identifying differences between the two results that fell outside of the combined Gumbel confidence interval. Almost no grid points showed a statistically significant difference between the two periods. This indicates that the Gumbel uncertainty dominates over any detectable shift in the extreme wind climate between the two halves.

Here in the Monte Carlo framework, each parameter was randomly sampled within an estimated 95% confidence interval using $\pm 1.96\sigma$, allowing comparisons across parameters. The method was repeated 100 times for each parameter. The following section outlines the approach taken to estimate the uncertainty for each variable.

## 4.1 Uncertainty associated with key parameters

### 4.1.1 Wind Speed

Wind speed is one of the few parameters for which uncertainties are provided within the IBTrACS documentation (IBTrACS Science Team, 2025), shown below in Table 5. As noted by the IBTrACS documentation, the uncertainty estimates are calculated from the contributions from the 3rd IBTrACS Workshop attendees. It takes into account the changes of forecasting methods over the year, changes in aircraft reconnaissance in the Western Pacific and Northern Atlantic and information provided from more than one agency for several basins. The absolute uncertainties change based on both year and ocean basin and are noted to be qualitative in nature.

While the absolute uncertainty is uniformly distributed, for this paper, the error distribution has been approximated as Gaussian, with the half-width, $a$, being equivalent to 1.96$\sigma$. Note that while the IEC standard outlines that parameters such as wind speed may follow a Weibull distribution, the present analysis assumes a Gaussian for the associated error rather than the parameter itself. This is a further step of approximation than that from BIPM and IEC and IFCC and ILAC and ISO and IUPAC and IUPAP and OIML (2008), which estimates the standard deviation of a uniform distribution as

$$\sigma = \frac{a}{\sqrt{3}} \tag{10}$$

All parameters for which the absolute uncertainty is provided, the same approximation will take place.

**Table 5.** IBTrACS Wind Speed Uncertainty (Knots)

| Year | Northern Atlantic | Western Pacific |
|---|---|---|
| 1973 - 1978 | ±20 $kt$ | ±20 $kt$ |
| 1978 - 1984 | ±15 $kt$ | ±20 $kt$ |
| 1984 - 1987 | ±10 $kt$ | ±10 $kt$ |
| 1987 - 1995 | ±10 $kt$ | ±15 $kt$ |
| 1995 - 2000 | ±10 $kt$ | ±10 $kt$ |
| 2000 - present | ±7 $kt$ | ±10 $kt$ |

### 4.1.2 Position

The position refers to the centre latitude-longitude location of a TC. The uncertainty for the position is also available from the IBTrACS documentation and is shown below in Table 6. Following the approximation within Section 4.1.1, the upper range of the absolute uncertainty is approximated as 1.96$\sigma$. For example, 1.96$\sigma$ = 40 km, therefore the latitude and longitude will be varied within ±40 km from their original position.

**Table 6.** IBTrACS Position Uncertainty (Kilometres)

| Intensity | Uncertainty |
|---|---|
| Weak TC (Winds $<$ 60 kt) | $\approx 30 - 40\ km$ |
| Moderate TC (60 kt $<$ Winds $<$ 100 kt) | $\approx 20 - 25\ km$ |
| Strong TC (Winds $>$ 100 kt) | $\approx 10 - 15\ km$ |

### 4.1.3 RMW

The RMW uncertainty has been calculated differently for the Northern Atlantic, where the ECUS lies, and the Western Pacific, where the Taiwan and Japan regions lie.

The ECUS will first be discussed. The US agencies' RMW uncertainty can be found in an online NOAA report https://www.nhc.noaa.gov/data/hurdat/hurdat2-format-atl-1851-2021.pdf, and a subset is shown below in Table 7. The report details extra information on the HURDAT2 dataset (Landsea and Franklin, 2013), which is supplied to IBTrACS.

For the ECUS region, only years from 2001 are included. Satellites carrying scatterometers were active for the entire period of analysis. Satellites providing near-global ocean coverage every 1-2 days include: QuikSCAT (1999–2009) (Hoffman and Leidner, 2005), ASCAT on MetOp-A (from 2006) (Figa-Saldaña et al., 2002; Wagner et al., 2013), and MetOp-B/C (from 2012/2018) (Wagner et al., 2013). Regions in which TCs occur are a priority for satellite coverage as many agencies rely on up-to-date coverage of TCs for modelling and accurate short-term forecasts (Kishtawal, 2016). Therefore, the absolute uncertainty was selected to be 12 nautical miles.

Given the approximation within Section 4.1.1, we define the absolute uncertainty, 12 nm equivalent to $1.96\sigma$, and vary the RMW within this range.

**Table 7.** US agencies IBTrACS Radius of Maximum Wind Uncertainty (Nautical Miles)

| Category and data available | Uncertainty |
|---|---|
| Category 1 or 2 Hurricane - Satellite/no scatterometer within 6 hr | $\pm 16\ nm$ |
| Category 1 or 2 Hurricane - Satellite/with scatterometer within 6 hr | $\pm 12\ nm$ |
| Category 1 or 2 Hurricane - Aircraft and satellite | $\pm 9\ nm$ |
| Category 1 or 2 Hurricane - U.S. landfall | $\pm 8\ nm$ |
| Category 3, 4, or 5 Hurricane - Satellite/no scatterometer within 6 hr $\pm 11\ nm$ | |
| Category 3, 4, or 5 Hurricane - Satellite/with scatterometer within 6 hr | $\pm 9\ nm$ |
| Category 3, 4, or 5 Hurricane - Aircraft and satellite | $\pm 5\ nm$ |
| Category 3, 4, or 5 Hurricane - U.S. landfall | $\pm 5\ nm$ |

For the Western Pacific, the outcome of converting the 50 km radius to the RMW is compared to available values from the US agencies within the Western Pacific region. From the differences, the mean standard deviation was 10567 m.

#### 4.1.4 Pressure

For the Northern Atlantic, Landsea and Franklin (2013) defines the absolute pressure uncertainty as 9.5 hPa for major TCs observed via satellite. For weaker TCs, such as category 1 or 2, the uncertainty is smaller. Therefore, using the uncertainty of 9.5 hPa is likely a conservative approach. Following the approximation within Section 4.1.1, we assign the absolute uncertainty, 9.5 hPa, as equivalent to $1.96\sigma$ and vary the pressure value within this range.

Within the Western Pacific, multiple agencies provide pressure values for the same TC time steps. These agencies include the JMA, HKO, CMA and US. Pressure values from these various agencies for each TC and time step were compared against each. The comparisons were used to calculate the mean standard deviation, which returned as 2.13 hPa and set as equivalent to $1.96\sigma$.

#### 4.1.5 $B$ parameter

The $B$ parameter is not provided directly in the IBTrACS dataset, but rather calculated from other variables. These variables are the central pressure and the maximum wind speed. As such, there is no documented uncertainty associated with the $B$ parameter. To estimate its uncertainty, the error propagation formula for correlated variables is applied:

$$\sigma_b^2 = \left(\frac{\partial b}{\partial V_{\max}}\right)^2 \sigma_{V_{\max}}^2 + \left(\frac{\partial b}{\partial P_c}\right)^2 \sigma_{P_c}^2 + 2\left(\frac{\partial b}{\partial V_{\max}}\right)\left(\frac{\partial b}{\partial P_c}\right) \mathrm{Cov}(V_{\max}, P_c) \tag{11}$$

This expression is derived from the first-order Taylor expansion, and its general application is described in Taylor (1997), while its application to meteorological contexts is described in detail in BIPM and IEC and IFCC and ILAC and ISO and IUPAC and IUPAP and OIML (2008).

The estimation relies on the assumption that the errors are small compared to the mean of the maximum wind speed and the pressure, the errors are unbiased and symmetric, and the errors are independent, or the covariance is accounted for, which is the case here.

In the Western Pacific, the uncertainty in wind speed varies over time, resulting in corresponding temporal variation in the $B$ parameter uncertainty. Once the variation in wind speed uncertainty over time is taken into account, for each time period, the mean $B$ parameter standard deviation is found and used. In contrast, for ECUS, only data from 2001 onward are used, during which a single wind speed uncertainty value applies. Consequently, a single $B$ parameter uncertainty estimate is reported for the ECUS region.

#### 4.1.6 Scaled Wind Speed

The Holland model returns the wind speed at the gradient level. To understand the wind speed impact on offshore infrastructure, the wind speed at a more relevant height should be calculated. The method of scaling the wind height from the gradient level to 100 m is detailed in Section 2.5. For validation, the wind speed was scaled to 10 m and the value was compared against IBTrACS. Using the difference between the two, the standard deviation could be calculated.

**Table 8.** B Parameter Standard Deviation (unitless)

| | Northern Atlantic | Western Pacific |
|---|---|---|
| 1973 - 1984 | na | 0.6999 |
| 1984 - 1987 | na | 0.3362 |
| 1987 - 1995 | na | 0.5433 |
| 1995 - 2001 | na | 0.3839 |
| 2001 - present | 0.2444 | 0.3839 |

**Table 9.** Scaled Wind Speed Standard Deviation (m $s^{-1}$)

| Taiwan | Japan | ECUS |
|---|---|---|
| 0.0171 m $s^{-1}$ | 0.0216 m $s^{-1}$ | 0.0393 m $s^{-1}$ |

### 4.1.7 Contributions to Total Uncertainty

To assess the influence of input parameters on the overall uncertainty of $U_{50}$, a variance-based sensitivity analysis is performed. This captures both individual effects and interaction terms. This approach is an approximation of the first and second order indices of Sobol (2001). Sobol's indices are widely used in sensitivity analysis (Dykes et al., 2014; Locatelli et al., 2017; Thapa and Missoum, 2022; Tsvetkova and Ouarda, 2019), however, this implementation follows a simpler approach: parameters are randomly sampled within their 95% confidence intervals.

Let $x_{p,m,i}$ be the value of parameter $p$ of Monte Carlo simulation $m$ at grid point $i$. Normalise each value at each grid point for each parameter:

$$\tilde{x}_{p,m,i} = \frac{x_{p,m,i} - \overline{x}_{p,i}}{\overline{x}_{p,i}}, \tag{12}$$

where $\overline{x}_{p,i}$ is the mean of all simulation values for grid point $i$ and parameter $p$. Firstly, the variation around the mean is calculated using $x_{p,m,i} - \overline{x}_{p,i}$. Following this, the variation is normalised by $\overline{x}_{p,i}$ to find the relative variation. The relative variation is used so that direct comparison can be made between parameters which have different units and scales of magnitude.

To calculate the variance (diagonal terms), which represent the individual parameters' contributions to total uncertainty, the following steps are taken:

Firstly, the variance term of parameter $p$ at a singular grid point $i$ is calculated by:

$$\mathrm{Var}_{p,i} = \frac{1}{N}\sum_{m} \tilde{x}^2_{p,m,i} \tag{13}$$

where N is the total number of simulations. The total variance from all parameters is defined as

$$\mathrm{Var}_{\text{diag total}} = \sum_{p,i} \mathrm{Var}_{p,i} \tag{14}$$

To account for the interaction terms, the covariance is computed, showing how parameter uncertainties interact. A positive value indicates that the parameters amplify each other's uncertainty, whereas a negative value indicates that the parameters partially counteract each other's uncertainty. The magnitude of the value indicates how strong this interaction is and how much the interaction contributes to the overall uncertainty. While each Monte Carlo simulation varies a singular parameter at each time, following the completion of the simulations, $\tilde{x}_{p,m,i}$ can be calculated for each parameter at each grid point. This allows the calculation of the covariance term between parameters $p_1$ and $p_2$ at a singular grid point $i$ and can be shown as:

$$\mathrm{Cov}_{p_1,p_2,i} = 2\frac{1}{N}\sum_{m}\tilde{x}_{p_1,m,i}\,\tilde{x}_{p_2,m,i} \tag{15}$$

where N is the total number of simulations. The contribution to the total off-diagonal variance from the covariance terms sum over all possible combinations:

$$\mathrm{Var}_{\text{off-diag total}} = \sum_{\substack{x,y\\x\neq y}}\sum_{i}\mathrm{Cov}_{p_x,p_y,i}, \tag{16}$$

where $x \neq y$ ensures that only distinct pairs of parameters are considered at each grid point.

The total variance can be defined as the sum of all variance and covariance terms and is $100\%$.

$$\mathrm{Var}_{\text{total}} = \mathrm{Var}_{\text{diag total}} + \mathrm{Var}_{\text{off-diag total}} \tag{17}$$

To calculate the percentage of total variation that each individual parameter and each interaction contributes towards is calculated by summing the variation for each individual parameter and each interaction across all grid points:

$$\mathrm{Var}_{p} = \sum_{i}\mathrm{Var}_{p,i} \tag{18}$$

$$\mathrm{Var}_{p_x,p_y} = \sum_{i}\mathrm{Cov}_{p_x,p_y,i}, \tag{19}$$

and dividing by the total variation from all parameters and interactions calculated in Equation 17.

### 4.2 Uncertainty Results

The mean $U_{50}$ and the standard deviation were calculated for each parameter for each set of 100 simulations. Each parameter was varied exclusively, while all others were held constant. Each parameter was varied within its approximate $95\%$ confidence interval. The regional results are presented in Fig.s 7, 8 and 9.

As shown in Tables 10, 11 and 12 across all regions, specific individual parameters dominate the overall uncertainty, rather than the interactions, where all parameter interactions contribute below $1\%$ in all cases.

The results shown in Tables 10 for Taiwan and 11 for Japan are, as expected, similar. They are close in proximity and have similar data restrictions. In both regions, the B parameter dominates the impact on the overall uncertainty. This could be attributed to the B parameter incorporating the uncertainty of two parameters, leading to a larger combined variance. The RMW has a smaller impact on the Taiwan and Japan regions; however, it contributes significantly to uncertainty within the ECUS region, particularly to the south, which will be further discussed in Section 5. Within the ECUS region, RMW, wind speed and the B parameter have similar uncertainty; however, the method takes into account the entire defined region. From Figure 9, it is clear the RMW uncertainty is primarily heightened in the southern half of the region. By breaking the region down further, the contribution to overall uncertainty would likely shift.

Wind speed uncertainty for all regions has a substantial impact, which is expected given its direct role in the $U_{50}$ calculation. Surprisingly, pressure uncertainty shows little influence in all three regions, suggesting that either the Holland model has low sensitivity to pressure variation or that the uncertainty associated with pressure is minimal. Scaling the wind speed and changing the latitude/longitude of the maximum wind speed appear to have a negligible impact on the overall uncertainty.

Examining the interaction contributions to the total uncertainty in Tables 10, 11 and 12, given that RMW, wind speed, and the B parameter are the biggest individual contributors to uncertainty, it is unsurprising that their interactions are the biggest contributions to uncertainty. Two notable features of the data are observed: (1) the largest interaction is between the RMW and B parameter in Taiwan, accounting for 7.2%; (2) the wind speed and B parameter interaction in Japan is negative, indicating that the uncertainty of these parameters partially counteract each other. However, given the confidence intervals associated with all interaction contributions, these effects could be close to negligible. Therefore, the primary focus should remain on the individual effects.

## 5 Discussion

There have been several methods developed in the literature to estimate the extreme winds in TC-prone areas.

Studies on this subject have previously used the IBTrACS data and covered the western North Pacific Ocean, with the winds at 10 m height, as in Ott (2006); Kong et al. (2024). This study differs from the previous by examining the entire IBTrACS data records from different agencies. The study area not only includes the western North Pacific Ocean, but also the east coast of the US. We examine both the wind speeds at 10 m, in order to compare with previous studies, but primarily wind speeds at 100 m, which is more relevant for modern wind turbines.

In this study, three regions were selected due to relatively high level of activities for offshore wind deployment: Taiwan, Japan and ECUS. Given a set of data restrictions, data from IBTrACS was used as input to the Holland model. The Holland model returned a wind field for each given data point. The wind speed was scaled down to 100 m using an adjusted roughness length. To estimate the adjusted roughness length, the Holland model output was scaled to 10 m and compared against the maximum wind speed from IBTrACS. The surface roughness, which resulted in the best fit to the IBTrACS values, was selected. The standard deviation of the fit was used within the Monte Carlo simulations. As the surface roughness was selected based on comparison against 10 m data, and this study primarily focuses on wind speeds at 100 m, there is potential for further

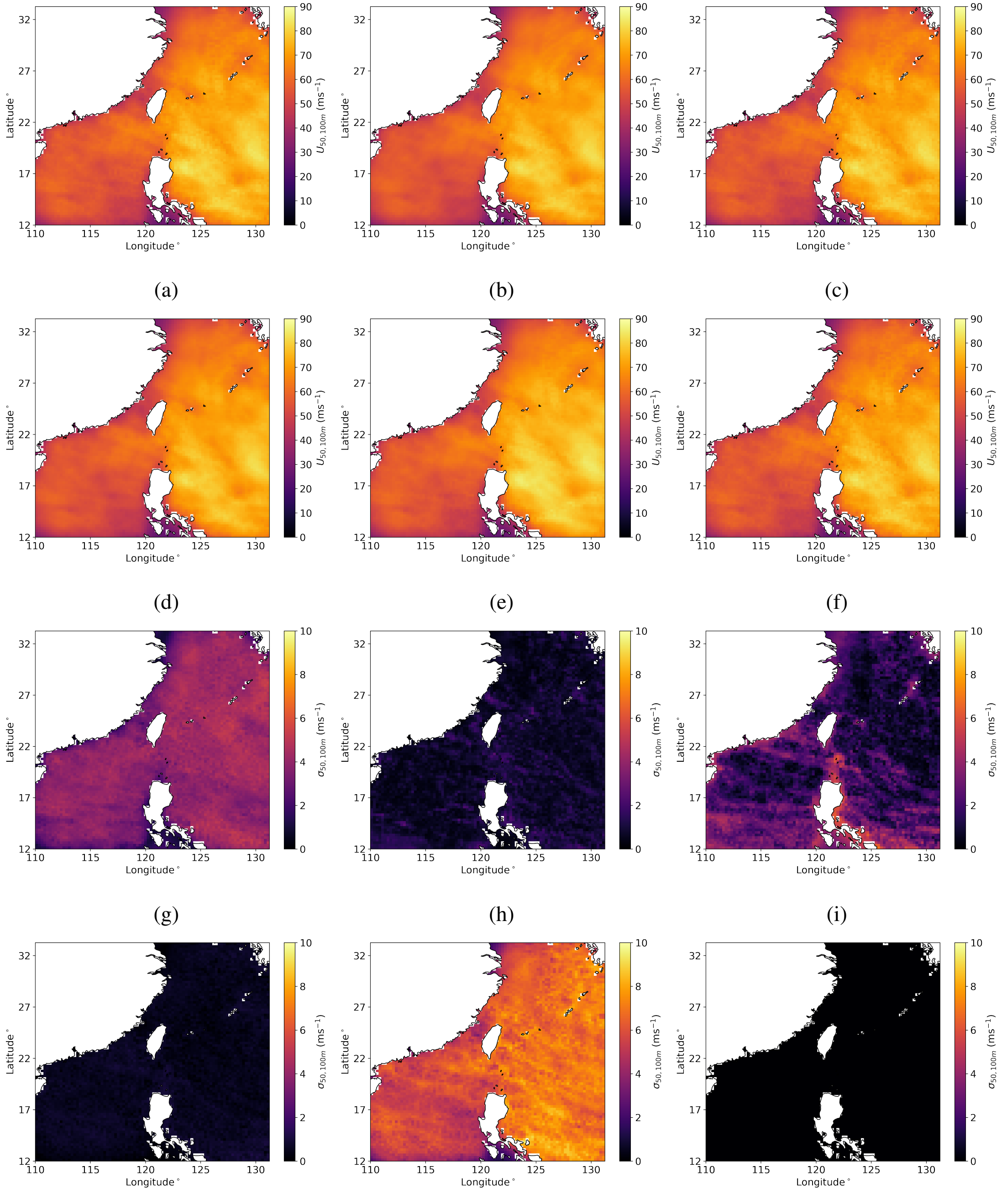

(a) (b) (c)

(d) (e) (f)

(g) (h) (i)

(j) (k) (l)

**Figure 7.** Monte Carlo Simulation results for Taiwan. (a)-(f) shows the mean wind speed from 100 simulations for each varying parameter and (g)-(l) shows the standard deviation from 100 simulations for each varying parameter. (a) and (g): Wind speed. (b) and (h): Eye coordinates. (c) and (i): RMW. (d) and (j): Pressure. (e) and (k): B parameter. (f) and (l): Scaled Wind Speed.

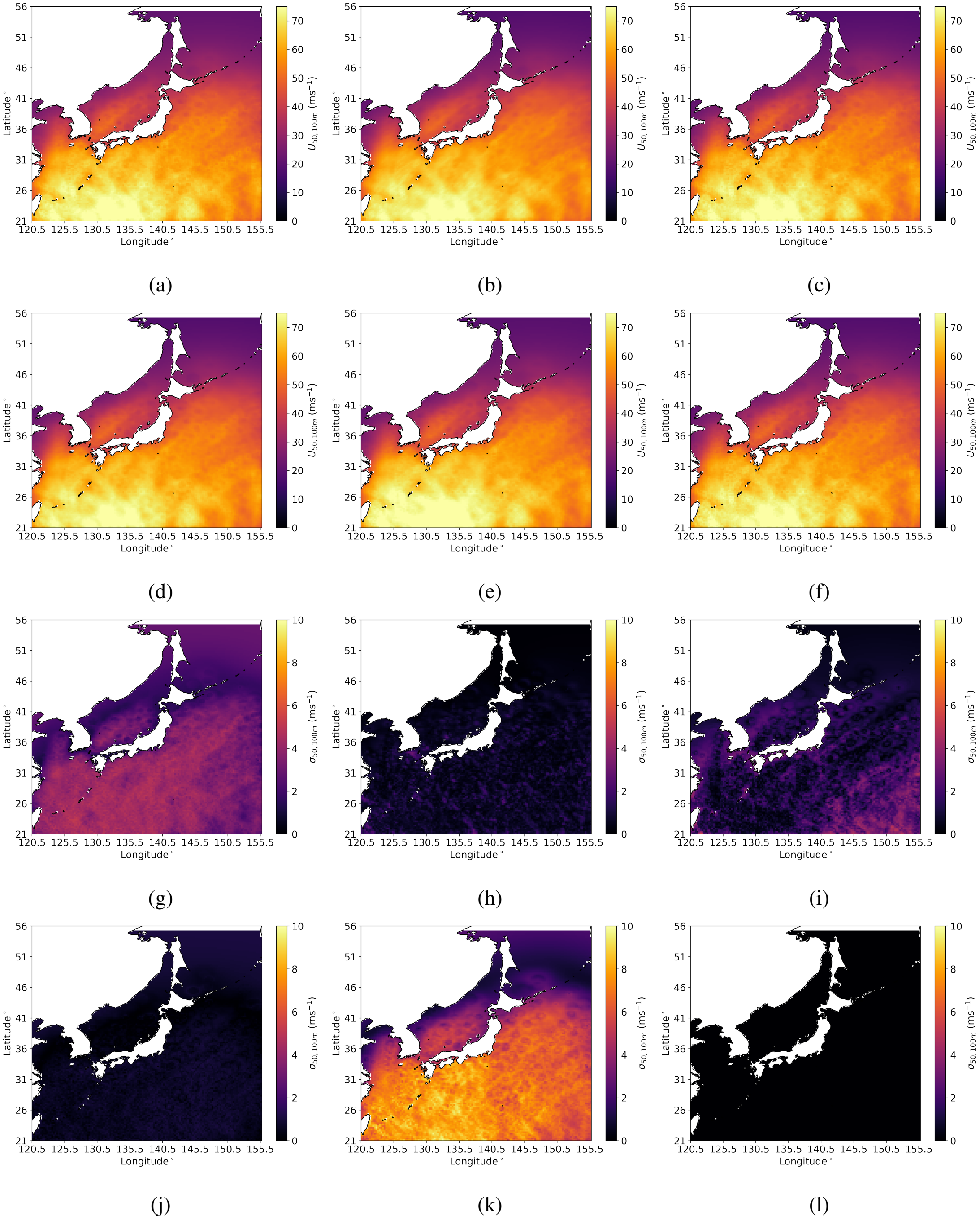

**Figure 8.** Monte Carlo Simulation results for Japan. (a)-(f) shows the mean wind speed from 100 simulations for each varying parameter and (g)-(l) shows the standard deviation from 100 simulations for each varying parameter. (a) and (g): Wind speed. (b) and (h): Eye coordinates. (c) and (i): RMW. (d) and (j): Pressure. (e) and (k): B parameter. (f) and (l): Scaled Wind Speed.

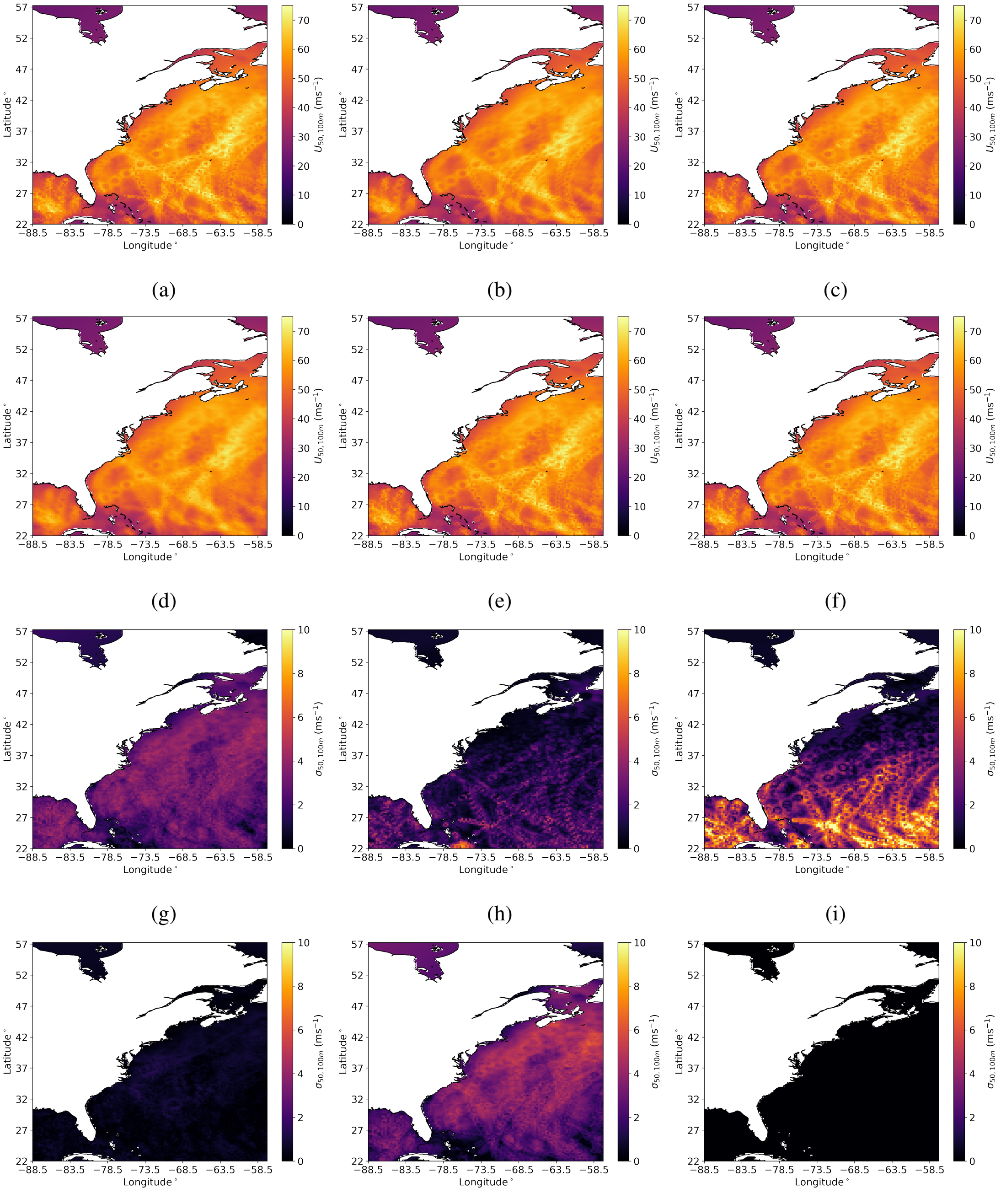

(a) (b) (c)

(d) (e) (f)

(g) (h) (i)

(j) (k) (l)

**Figure 9.** Monte Carlo Simulation results for ECUS. (a)-(f) shows the mean wind speed from 100 simulations for each varying parameter and (g)-(l) shows the standard deviation from 100 simulations for each varying parameter. (a) and (g): Wind speed. (b) and (h): Eye coordinates. (c) and (i): RMW. (d) and (j): Pressure. (e) and (k): B parameter. (f) and (l): Scaled Wind Speed.

**Table 10.** Contribution to Total Uncertainty in Taiwan (Percentage)

| Parameter | Percentage | Std | Interaction | Percentage | Std |
|---|---|---|---|---|---|
| Wind Speed | 23.0% | 7.0% | Position | 0.1% | 0.7% |
| | | | RMW | 1.2% | 1.0% |
| | | | Pressure | 0.3% | 0.2% |
| | | | B Parameter | 1.8% | 2.4% |
| | | | Scaled Wind Speed | 0.0% | 0.0% |
| Position | 1.2% | 1.21% | RMW | -0.3% | 0.5% |
| | | | Pressure | -0.0% | 0.1% |
| | | | B Parameter | -0.0% | 0.93% |
| | | | Scaled Wind Speed | 0.0% | 0.0% |
| RMW | 8.3% | 9.8% | Pressure | 0.1% | 0.1% |
| | | | B Parameter | 7.2% | 5.1% |
| | | | Scaled Wind Speed | 0.0% | 0.0% |
| Pressure | 0.5% | 0.3% | B Parameter | 0.7% | 0.4% |
| | | | Scaled Wind Speed | 0.0% | 0.0% |
| B Parameter | 56.7% | 8.7% | Scaled Wind Speed | 0.0% | 0.0% |
| Scaled Wind Speed | 0.0% | 0.0% | | | |

uncertainty to arise, which has not been taken into account. Following the scaling of the wind speed to 100 m, at each grid point, the annual maxima was calculated. Lastly, using the Gumbel distribution, $U_{50}$ was calculated as the final result.

Monte Carlo simulations were used for uncertainty analysis, where the parameters including wind speed, position, RMW, pressure, $B$ parameter and scaled wind speed were randomly varied 100 times within their 95% confidence interval range. How well the method performed in each of the regions and the associated errors can be attributed to regional differences in TC characteristics.

The method seemed to work well for the Taiwan region by comparison against other studies. The maximum wind speed of $\mathrm{U}_{50}$ at 10 m from this study was 0.7 $\mathrm{ms}^{-1}$ larger than that from Ott (2006), 2.3 $\mathrm{ms}^{-1}$ larger than Kong et al. (2024) and 0.3 $\mathrm{ms}^{-1}$ smaller than that in Larsén and Ott (2022). It also presented a similar spatial distribution of winds in which the maximum winds occur to the north-east of the Philippians, high wind speeds extend north, while gradually weakening towards the south of Japan and weaker wind speeds to the west of the Philippians compare to the east of the Philippians. The three studies previously mentioned also included the Japan region, also showing the peak wind speeds occurring to the south of Japan, gradually weakening as the latitude increases. The ECUS region differed from the previous two by deviating from expectations.

Here, we discuss the differences between the regions, primarily why the ECUS looks to be less reliable than the other regions.

**Table 11.** Contribution to Total Uncertainty in Japan (Percentage)

| Parameter | Percentage | Std | Interaction | Percentage | Std |
|---|---|---|---|---|---|
| Wind Speed | 29.2% | 17.7% | Position | 0.4% | 1.0% |
| | | | RMW | -0.3% | 4.7% |
| | | | Pressure | -0.3% | 1.0% |
| | | | B Parameter | -3.4% | 3.1% |
| | | | Scaled Wind Speed | 0.0% | 0.0% |
| Position | 1.0% | 1.25% | RMW | 0.2% | 0.6% |
| | | | Pressure | -0.1% | 0.8% |
| | | | B Parameter | -0.2% | 1.0% |
| | | | Scaled Wind Speed | 0.0% | 0.0% |
| RMW | 6.2% | 6.4% | Pressure | -0.0% | 0.1% |
| | | | B Parameter | 4.5% | 4.0% |
| | | | Scaled Wind Speed | 0.0% | 0.0% |
| Pressure | 2.6% | 4.3% | B Parameter | 0.8% | 1.8% |
| | | | Scaled Wind Speed | 0.0% | 0.0% |
| B Parameter | 59.5% | 16.9% | Scaled Wind Speed | 0.0% | 0.0% |
| Scaled Wind Speed | 0.0% | 0.0% | | | |

Firstly, the focus will be on the prominent appearance of specific tracks within the ECUS region in comparison to the much weaker appearance in Japan and Taiwan. By evaluating the data availability of these regions, it becomes apparent that, per year on average, the ECUS region has the least amount of data points, which can be calculated from Table 2. The smaller data count is then coupled with the wider spatial spread of data points, as shown in Fig. 6c. Following this, the ECUS neighbouring grid points can exhibit larger variations in annual maximum wind speeds compared to Japan and Taiwan. In Taiwan and Japan the spatial gradients are generally smoother. The Gumbel distribution is fitted directly to the annual maxima at each grid point, meaning that, the larger differences in annual maxima for neighbouring grid points will produce different $U_{50}$ estimations, causing the fragmented appearance.

Secondly, within the ECUS, it was also expected to see the highest wind speeds consistently appear at lower latitudes due to the correlation of lower latitudes and smaller RMW (Kimball and Mulekar, 2004; Vickery and Wadhera, 2008; Pérez-Alarcón et al., 2021) which indicate stronger winds (Kimball and Mulekar, 2004; Chavas and Knaff, 2022). While this feature is not apparent, it can be explained through examination of the Holland model.

The Holland model is known to underestimate wind speeds at distances two to three times the RMW (Willoughby and Rahn, 2004) as it rapidly decreases the wind speed at these distances. The limitation becomes more pronounced when the RMW is small: the area at two to three times the RMW is still relatively close to the TC's centre, where wind speeds remain high. Therefore, the Holland model's tendency to underestimate winds reduces the accuracy of capturing the extreme wind field from

**Table 12.** Contribution to Total Uncertainty in ECUS (Percentage)

| Parameter | Percentage | Std | Interaction | Percentage | Std |
|---|---|---|---|---|---|
| Wind Speed | 23.5% | 11.2% | Position | 0.1% | 2.1% |
| | | | RMW | 2.3% | 2.2% |
| | | | Pressure | 0.3% | 0.3% |
| | | | B Parameter | 2.7% | 1.6% |
| | | | Scaled Wind Speed | 0.0% | 0.0% |
| Position | 6.94% | 8.03% | RMW | 0.2% | 4.19% |
| | | | Pressure | 0.0% | 0.5% |
| | | | B Parameter | 0.2% | 2.1% |
| | | | Scaled Wind Speed | 0.0% | 0.1% |
| RMW | 31.0% | 26.8% | Pressure | 0.1% | 0.5% |
| | | | B Parameter | 1.31% | 1.61% |
| | | | Scaled Wind Speed | 0.0% | 0.0% |
| Pressure | 1.01% | 1.5% | B Parameter | -0.5% | 0.7% |
| | | | Scaled Wind Speed | 0.0% | 0.0% |
| B Parameter | 30.8% | 20.1% | Scaled Wind Speed | 0.0% | 0.0% |
| Scaled Wind Speed | 0.0% | 0.0% | | | |

small-RMW TCs. This problem further exacerbates the first issue, which is why at the lower latitudes we see smaller areas of high wind speeds.

In contrast, TCs which track further north in the ECUS region often have larger RMW (Kimball and Mulekar, 2004) and typically have lower maximum wind speeds (Kimball and Mulekar, 2004; Chavas and Knaff, 2022). While the Holland model may still underestimate the wind speeds at two to three times the RMW, this corresponds to a distance much further from the TC's core, where the wind speeds have already weakened. Due to this, the underestimation primarily affects less critical regions of the wind field for this study, while the important core winds are captured reasonably well.

We do not see the spatial fragmentation, to the same extent, occurring within the Taiwan and Japan regions, supporting the theory that the key of the issue is the smaller dataset in the ECUS region. While the underestimation of winds outside two to three times the RMW will still be present, the number of data points in Taiwan and Japan is higher, and it is consolidated into a smaller region in comparison to the ECUS . The annual maxima displays reduced spatial variability between neighbouring points which is reflected in the Gumbel distribution and the $U_{50}$ estimation. Therefore, it is the combination of a smaller dataset in the ECUS than Taiwan and Japan and a consistent area where small-RMW TCs occur that makes this method less reliable for the ECUS region.

This rationalisation is supported by the uncertainty analysis. As shown in Figure 9, the RMW within the southern half of the ECUS region plays an important role within the uncertainty, whereas its influence in the Taiwan and Japan regions is much smaller, (Fig.s 7 and 8), even though the same methodology is applied. The larger uncertainty within the Taiwan and Japan regions comes from the B parameters. These differences reflect how regional TC characteristics influence outcomes in each of the regions.

Given that many parameters are involved in this method, Monte Carlo simulations were effective to address the associated uncertainty. However, the diversity of uncertainties within the IBTrACS data makes this a challenging analysis. While the uncertainty analysis undertaken in this study may not capture all possible uncertainties, results could provide an indication of the potential range of uncertainty and which parameters affect uncertainty the most. An uncertainty which has not been quantified is the results of the sampling resolution of IBTrACS. When a TC is positioned between two consecutive track points, there is no information available and therefore there are spatial gaps in the track. This could lead to under-representation of peak winds, particularly where storms move quickly or data is sparse. As such, this is more likely to affect the results within the ECUS region than Taiwan or Japan regions. Interpolating the track to a finer temporal resolution could be attempted, however, it would require assumptions about the TC evolution between observations. This in turn which would risk the introduction of greater uncertainty than that of the sampling gap. A secondary uncertainty which has not been addressed is the potential impact of climate variability on the results. While all available data has been used, it may not represent the long-term TC climate if the period coincides with an active or in-active phase of natural variability. A period of enhanced TC activity could inflate the annual maxima which is fed into the Gumbel distribution which could return a higher $U_{50}$. A suppressed period would do the opposite. Although the split-half analysis revealed that the Gumbel uncertainty dominates over any detectable shift in the extreme wind climate between sub-periods, climatological variability remains an unquantified source of uncertainty.

Data availability in the ECUS is heavily limited by the availability of parameter RMW, which is only recorded from 2001 onward. One way to extend the availability is to estimate the RMW using a reanalysis dataset and integrate it with IBTrACS. Another potential option is to use a synthetic dataset, such as STORM (Bloemendaal et al., 2020b) for the analysis. A third approach is to generate a synthetic tropical cyclone database following the methodology outlined in Annex J of the IEC 61400-1 standard. However, this study was intended to specifically focus on IBTrACS data. To better capture the extreme winds from small-RMW TCs, a variation of the Holland model could be used that captures the differences between the inner core and the outer regions, as is suggested by Chavas et al. (2015).

## 6 Conclusions

Overall, this analysis demonstrates that combining IBTrACS data with the Holland model and the Gumbel distribution can provide a viable approach for estimating $U_{50}$ in some TC-affected regions. This approach is most robust in regions with substantial, spatially consolidated datasets and where RMW are not consistently small, such as in Taiwan and Japan. But in regions, like the ECUS, in which the dataset does not fit this criteria, the method shows limitations. Monte Carlo simulations were effective in quantifying uncertainties, highlighting the influence of region specific TC characteristics on the results. While some uncertainties could remain unaccounted for, the approach offers insight into extreme wind estimation at heights relevant for modern wind turbines.

The key findings of this study are summarized as follows:

- The method integrates IBTrACS data, the Holland model, and the Gumbel distribution to estimate extreme wind speeds $\mathrm{U}_{50}$ at 10 m and 100 m, complementing previous studies.
- Data for the Taiwan and Japan regions is substantial and consolidated into a specific area allowing for smooth spatial gradients in the annual maxima when comparing neighbouring grid points, leading to more smooth $\mathrm{U}_{50}$ estimation across the regions.
- ECUS shows larger variability between neighbouring grid points due to smaller, more widely spread data points which is exacerbated at the lower latitudes due to a higher occurrence of small-RMW TCs.
- The Holland model underestimates wind speeds at distances two to three times RMW, particularly affecting small-RMW TCs and contributing to spatial fragmentation in ECUS.
- Monte Carlo simulations capture the uncertainty from input parameters, though some sources of uncertainty remain unquantified.

Future work could explore the use of alternative parametric models to better capture regional variations in TC characteristics and specifically improve performance within the ECUS region. In addition, applying the existing methodology while using larger datasets may reduce uncertainty and could provide reasonable results within the ECUS region. Using the existing methodology while comparing results using different variations of datasets would enable a systematic comparison between historical TC records and synthetic databases which represent a broader range of plausible, but unobserved, events. Finally, incorporating the influence of climate variability into the uncertainty framework is an important extension, as the current $U_{50}$ does not account for this.

*Data availability.* The IBTrACS data is available at https://www.ncei.noaa.gov/products/international-best-track-archive, https://doi.org/10.25921/82ty-9e16 (Gahtan et al., 2024), https://doi.org/10.1175/2009BAMS2755.1 (Knapp et al., 2010).

## References

Abild, J.: Application of the Wind Atlas Method to Extremes of Wind Climatology, Denmark. Forskningscenter Risoe. Risoe-R, Risø National Laboratory, Roskilde, Denmark, ISBN 87-550-1438-0, 1994.

Anastasiades, G. and McSharry, P. E.: Extreme Value Analysis for Estimating 50 Year Return Wind Speeds from Reanalysis Data, Wind Energy, 17, 1231–1245, https://doi.org/10.1002/we.1630, 2014.

Arthur, W. C.: A Statistical–Parametric Model of Tropical Cyclones for Hazard Assessment, Natural Hazards and Earth System Sciences, 21, 893–916, https://doi.org/10.5194/nhess-21-893-2021, 2021.

BIPM and IEC and IFCC and ILAC and ISO and IUPAC and IUPAP and OIML: Evaluation of Measurement Data — Guide to the Expression of Uncertainty in Measurement, Tech. Rep. JCGM 100:2008, Joint Committee for Guides in Metrology, https://doi.org/10.59161/JCGM100-2008E, 2008.

Blackadar, A. K. and Tennekes, H.: Asymptotic Similarity in Neutral Barotropic Planetary Boundary Layers, Journal of the Atmospheric Sciences, 25, 1015–1020, https://doi.org/10.1175/1520-0469(1968)025<1015:ASINBP>2.0.CO;2, 1968.

Bloemendaal, N., de Moel, H., Muis, S., Haigh, I. D., and Aerts, J. C. J. H.: Estimation of Global Tropical Cyclone Wind Speed Probabilities Using the STORM Dataset, Scientific Data, 7, 377, https://doi.org/10.1038/s41597-020-00720-x, 2020a.

Bloemendaal, N., Haigh, I. D., de Moel, H., Muis, S., Haarsma, R. J., and Aerts, J. C. J. H.: Generation of a Global Synthetic Tropical Cyclone Hazard Dataset Using STORM, Scientific Data, 7, 40, https://doi.org/10.1038/s41597-020-0381-2, 2020b.

Cao, X., Wu, R., Jiang, X., Dai, Y., Wang, P., Lin, C., Deng, D., Sun, Y., Wu, L., Chen, S., Wang, Y., and Xiao, X.: Future Changes in Tropical Cyclone Tracks over the Western North Pacific under Climate Change, npj Climate and Atmospheric Science, 8, 148, https://doi.org/10.1038/s41612-025-01036-6, 2025.

Chan, K. T. F. and Chan, J. C. L.: Size and Strength of Tropical Cyclones as Inferred from QuikSCAT Data, Monthly Weather Review, 140, 811–824, https://doi.org/10.1175/MWR-D-10-05062.1, 2012.

Chavas, D. R. and Knaff, J. A.: A Simple Model for Predicting the Tropical Cyclone Radius of Maximum Wind from Outer Size, Weather and Forecasting, 37, 563–579, https://doi.org/10.1175/WAF-D-21-0103.1, 2022.

Chavas, D. R., Lin, N., and Emanuel, K.: A Model for the Complete Radial Structure of the Tropical Cyclone Wind Field. Part I: Comparison with Observed Structure, Journal of the Atmospheric Sciences, 72, 3647–3662, https://doi.org/10.1175/JAS-D-15-0014.1, 2015.

Chen, C.-H. and Su, N.-J.: Global Trends and Characteristics of Offshore Wind Farm Research over the Past Three Decades: A Bibliometric Analysis, Journal of Marine Science and Engineering, 10, 1339, https://doi.org/10.3390/jmse10101339, 2022.

Commission, I. E.: Design Requirements, Wind Energy Generation Systems / International Electrotechnical Commission, International Electrotechnical Commission, Geneva, Switzerland, edition 4.0 edn., ISBN 978-2-8322-6253-5, 2019.

Díaz, H. and Guedes Soares, C.: Review of the Current Status, Technology and Future Trends of Offshore Wind Farms, Ocean Engineering, 209, 107 381, https://doi.org/10.1016/j.oceaneng.2020.107381, 2020.

Dykes, K., Ning, A., King, R., Graf, P., Scott, G., and Veers, P. S.: Sensitivity Analysis of Wind Plant Performance to Key Turbine Design Parameters: A Systems Engineering Approach, in: 32nd ASME Wind Energy Symposium, American Institute of Aeronautics and Astronautics, National Harbor, Maryland, ISBN 978-1-62410-313-1, https://doi.org/10.2514/6.2014-1087, 2014.

Fang, P., Ye, G., and Yu, H.: A Parametric Wind Field Model and Its Application in Simulating Historical Typhoons in the Western North Pacific Ocean, Journal of Wind Engineering and Industrial Aerodynamics, 199, 104 131, https://doi.org/10.1016/j.jweia.2020.104131, 2020.

Fei, R., Xu, J., Wang, Y., and Yang, C.: Factors Affecting the Weakening Rate of Tropical Cyclones over the Western North Pacific, Monthly Weather Review, 148, 3693–3712, https://doi.org/10.1175/MWR-D-19-0356.1, 2020.

Figa-Saldaña, J., Wilson, J. J. W., Attema, E., Gelsthorpe, R., Drinkwater, M. R., and Stoffelen, A.: The Advanced Scatterometer (ASCAT) on the Meteorological Operational (MetOp) Platform: A Follow On for European Wind Scatterometers, Canadian Journal of Remote Sensing, 28, 404–412, https://doi.org/10.5589/m02-035, 2002.

Franklin, J. L., Black, M. L., and Valde, K.: GPS Dropwindsonde Wind Profiles in Hurricanes and Their Operational Implications, Weather and Forecasting, 18, 32–44, https://doi.org/10.1175/1520-0434(2003)018<0032:GDWPIH>2.0.CO;2, 2003.

Gahtan, J., Knapp, K. R., Schreck, C. J. I., Diamond, H. J., Kossin, J. P., and Kruk, M. C.: International Best Track Archive for Climate Stewardship (IBTrACS) Project, Version 4.01, https://www.ncei.noaa.gov/access/metadata/landing-page/bin/iso?id=gov.noaa.ncdc:C01552, https://doi.org/10.25921/82ty-9e16, last Modified: 2024-08-14, NOAA National Centers for Environmental Information, 2024.

Gandoin, R. and Garza, J.: Underestimation of Strong Wind Speeds Offshore in ERA5: Evidence, Discussion and Correction, Wind Energy Science, 9, 1727–1745, https://doi.org/10.5194/wes-9-1727-2024, 2024.

Guo, J., Wang, S., He, X., Song, J., Fu, Y., and Cai, Y.: Interannual Characteristics of Tropical Cyclones in Northwestern Pacific Region in Context of Warm Pool and Monsoon Troughs, Journal of Marine Science and Engineering, 13, 334, https://doi.org/10.3390/jmse13020334, 2025.

Harper, B. A., Kepert, J. D., and Ginger, J. D.: Guidelines for Converting Between Various Wind Averaging Periods in Tropical Cyclone Conditions, Tech. Rep. WMO–TD–No. 1555, World Meteorological Organization, https://library.wmo.int/viewer/48652, 2010.

He, Y., Fu, J., Chan, P. W., Li, Q., Shu, Z., and Zhou, K.: Reduced Sea-Surface Roughness Length at a Coastal Site, Atmosphere, 12, 991, https://doi.org/10.3390/atmos12080991, 2021.

Hoffman, R. N. and Leidner, S. M.: An Introduction to the Near–Real–Time QuikSCAT Data, Weather and Forecasting, 20, 476–493, https://doi.org/10.1175/WAF841.1, 2005.

Holland, G. J.: An Analytic Model of the Wind and Pressure Profiles in Hurricanes, Monthly Weather Review, 108, 1212–1218, https://doi.org/10.1175/1520-0493(1980)108<1212:AAMOTW>2.0.CO;2, 1980.

Hu, X., Fang, G., Yang, J., Zhao, L., and Ge, Y.: Simplified Models for Uncertainty Quantification of Extreme Events Using Monte Carlo Technique, Reliability Engineering & System Safety, 230, 108 935, https://doi.org/10.1016/j.ress.2022.108935, 2023.

IBTrACS Science Team: International Best Track Archive for Climate Stewardship (IBTrACS): Technical Documentation (Version 04r01), Tech. rep., NOAA National Centers for Environmental Information, https://www.ncei.noaa.gov/sites/default/files/2025-04/IBTrACS_version4r01_Technical_Details.pdf, accessed: 2025-09-01, 2025.

Imberger, M., Larsén, X. G., and Davis, N.: Global Atlas for Siting Parameters Ocean and Coasts: Ensemble Calculation of 50-Year Return Winds, DTU Wind and Energy Systems E-0244, https://doi.org/10.11581/DTU.00000321, 2024.

Ishihara, T. and Yamaguchi, A.: Prediction of the Extreme Wind Speed in the Mixed Climate Region by Using Monte Carlo Simulation and Measure–Correlate–Predict Method, Wind Energy, 18, 171–186, https://doi.org/10.1002/we.1693, 2015.

Kimball, S. K. and Mulekar, M. S.: A 15-Year Climatology of North Atlantic Tropical Cyclones. Part I: Size Parameters, Journal of Climate, 17, 3555–3575, https://doi.org/10.1175/1520-0442(2004)017<3555:AYCONA>2.0.CO;2, 2004.

Kishtawal, C. M.: Use of Satellite Observations in Tropical Cyclone Studies, in: Advanced Numerical Modeling and Data Assimilation Techniques for Tropical Cyclone Prediction, edited by Mohanty, U. C. and Gopalakrishnan, S. G., pp. 35–47, Springer Netherlands, Dordrecht, ISBN 978-94-024-0896-6, https://doi.org/10.5822/978-94-024-0896-6_2, 2016.

Knaff, J. A., Sampson, C. R., Kucas, M. E., Slocum, C. J., Brennan, M. J., Meissner, T., Ricciardulli, L., Mouche, A., Reul, N., Morris, M., Chirokova, G., and Caroff, P.: Estimating Tropical Cyclone Surface Winds: Current Status, Emerging Technologies, Historical Evolution, and a Look to the Future, Tropical Cyclone Research and Review, 10, 125–150, https://doi.org/10.1016/j.tcrr.2021.09.002, 2021.

Knapp, K. R., Kruk, M. C., Levinson, D. H., Diamond, H. J., and Neumann, C. J.: The International Best Track Archive for Climate Stewardship (IBTrACS): Unifying Tropical Cyclone Data, Bulletin of the American Meteorological Society, 91, 363–376, https://doi.org/10.1175/2009BAMS2755.1, 2010.

Kong, L., Zhang, X., Wu, H., and Li, Y.: Estimation of Extreme Wind Speeds with Different Return Periods in the Northwest Pacific, Meteorological Applications, 31, e70 012, https://doi.org/10.1002/met.70012, 2024.

Kossin, J. P.: Validating Atmospheric Reanalysis Data Using Tropical Cyclones as Thermometers, Bulletin of the American Meteorological Society, 96, 1089–1096, https://doi.org/10.1175/BAMS-D-14-00180.1, 2015.

Kossin, J. P.: A Global Slowdown of Tropical-Cyclone Translation Speed, Nature, 558, 104–107, https://doi.org/10.1038/s41586-018-0158-3, 2018.

Landsea, C. W. and Franklin, J. L.: Atlantic Hurricane Database Uncertainty and Presentation of a New Database Format, Monthly Weather Review, 141, 3576–3592, https://doi.org/10.1175/MWR-D-12-00254.1, publisher: American Meteorological Society, 2013.

Larsén, X. G. and Ott, S.: Adjusted Spectral Correction Method for Calculating Extreme Winds in Tropical-Cyclone-Affected Water Areas, Wind Energy Science, 7, 2457–2468, https://doi.org/10.5194/wes-7-2457-2022, 2022.

Larsén, X. G., Mann, J., Rathmann, O., and Jørgensen, H. E.: Uncertainties of the 50-year wind from short time series using generalized extreme value distribution and generalized Pareto distribution, Wind Energy, 18, 59–74, https://doi.org/10.1002/we.1683, 2015.

Li, J., Tian, Q., Shen, Z., Xu, Y., Yan, Z., Li, M., Zhu, C., Xue, J., Lin, Z., Yang, Y., and Zeng, L.: Fidelity of Global Tropical Cyclone Activity in a New Reanalysis Dataset (CRA40), Meteorological Applications, 31, e70 009, https://doi.org/10.1002/met.70009, 2024.

Liu, G., Jiang, S., Zheng, M., Lin, S., Kong, Y., and Zhan, P.: A Global ERA5-based Tropical Cyclone Wind Field Dataset Enhanced by Integrated Parametric Correction Methods, Scientific Data, 12, 1429, https://doi.org/10.1038/s41597-025-05789-w, 2025.

Locatelli, T., Tarantola, S., Gardiner, B., and Patenaude, G.: Variance-Based Sensitivity Analysis of a Wind Risk Model – Model Behaviour and Lessons for Forest Modelling, Environmental Modelling & Software, 87, 84–109, https://doi.org/10.1016/j.envsoft.2016.10.010, 2017.

Mavromatis, T.: Evaluation of Reanalysis Data in Meteorological and Climatological Applications: Spatial and Temporal Considerations, Water, 14, 2769, https://doi.org/10.3390/w14172769, 2022.

Metropolis, N. and Ulam, S.: The Monte Carlo Method, Journal of the American Statistical Association, 44, 335–341, https://doi.org/10.2307/2280232, 1949.

Morin, G., Boudreault, M., and García-Franco, J. L.: A Global Multi-Source Tropical Cyclone Precipitation (MSTCP) Dataset, Scientific Data, 11, 609, https://doi.org/10.1038/s41597-024-03395-w, 2024.

Mortlock, T. R., Metters, D., Soderholm, J., Maher, J., Lee, S. B., Boughton, G., Stewart, N., Zavadil, E., and Goodwin, I. D.: Extreme Water Levels, Waves and Coastal Impacts During a Severe Tropical Cyclone in Northeastern Australia: A Case Study for Cross-Sector Data Sharing, Natural Hazards and Earth System Sciences, 18, 2603–2623, https://doi.org/10.5194/nhess-18-2603-2018, 2018.

Ott, S.: Extreme Winds in the Western North Pacific, Denmark. Forskningscenter Risoe. Risoe-R, Risø National Laboratory, Roskilde, ISBN 87-550-3500-0, 2006.

Park, D.-S. R., Ho, C.-H., Kim, J.-H., and Kim, H.-S.: Spatially Inhomogeneous Trends of Tropical Cyclone Intensity over the Western North Pacific for 1977–2010, Journal of Climate, 26, 5088–5101, https://doi.org/10.1175/JCLI-D-12-00386.1, 2013.

Powell, M. D. and Reinhold, T. A.: Tropical Cyclone Destructive Potential by Integrated Kinetic Energy, Bulletin of the American Meteorological Society, 88, 513–526, https://doi.org/10.1175/BAMS-88-4-513, 2007.

Pérez-Alarcón, A., Sorí, R., Fernández-Alvarez, J. C., Nieto, R., and Gimeno, L.: Comparative Climatology of Outer Tropical Cyclone Size Using Radial Wind Profiles, Weather and Climate Extremes, 33, 100 366, https://doi.org/10.1016/j.wace.2021.100366, 2021.

Rossby, C.-G. and Montgomery, R. B.: The Layer of Frictional Influence in Wind and Ocean Currents, Physics of Fluids, https://hdl.handle.net/1912/1157, 1935.

Schreck, C. J., Knapp, K. R., and Kossin, J. P.: The Impact of Best Track Discrepancies on Global Tropical Cyclone Climatologies Using IBTrACS, Monthly Weather Review, 142, 3881–3899, https://doi.org/10.1175/MWR-D-14-00021.1, 2014.

Sobol, I. M.: Global Sensitivity Indices for Nonlinear Mathematical Models and Their Monte Carlo Estimates, Mathematics and Computers in Simulation, 55, 271–280, https://doi.org/10.1016/S0378-4754(00)00270-6, 2001.

Taylor, J. R.: An introduction to error analysis: the study of uncertainties in physical measurements, University Science Books, Sausalito, Calif, second edition. edn., ISBN 0-935702-42-3, 1997.

Thapa, M. and Missoum, S.: Uncertainty Quantification and Global Sensitivity Analysis of Composite Wind Turbine Blades, Reliability Engineering & System Safety, 222, 108 354, https://doi.org/10.1016/j.ress.2022.108354, 2022.

Troen, I. and Petersen, E. L.: European Wind Atlas, Risø National Laboratory, Roskilde, ISBN 978-87-550-1482-4, 1989.

Tsvetkova, O. and Ouarda, T. B. M. J.: Quasi-Monte Carlo Technique in Global Sensitivity Analysis of Wind Resource Assessment with a Study on UAE, Journal of Renewable and Sustainable Energy, 11, 053 303, https://doi.org/10.1063/1.5120035, 2019.

Vickery, P. J. and Wadhera, D.: Statistical Models of Holland Pressure Profile Parameter and Radius to Maximum Winds of Hurricanes from Flight-Level Pressure and H*Wind Data, Journal of Applied Meteorology and Climatology, 47, 2497–2517, https://doi.org/10.1175/2008JAMC1837.1, 2008.

Vickery, P. J., Wadhera, D., Twisdale, L. A., and Lavelle, F. M.: U.S. Hurricane Wind Speed Risk and Uncertainty, Journal of Structural Engineering, 135, 301–320, https://doi.org/10.1061/(ASCE)0733-9445(2009)135:3(301), 2009.

Wagner, W., Hahn, S., Kidd, R., Melzer, T., Bartalis, Z., Hasenauer, S., Figa-Saldaña, J., de Rosnay, P., Jann, A., Schneider, S., Komma, J., Kubu, G., Brugger, K., Aubrecht, C., Züger, J., Gangkofner, U., Kienberger, S., Brocca, L., Wang, Y., Blöschl, G., Eitzinger, J., and Steinnocher, K.: The ASCAT Soil Moisture Product: A Review of its Specifications, Validation Results, and Emerging Applications, Meteorologische Zeitschrift, 22, 5–33, https://doi.org/10.1127/0941-2948/2013/0399, 2013.

Wang, Y., Wu, X., Jiang, L., Zheng, F., and Brune, S.: Editorial: Recent Advances in Climate Reanalysis, Frontiers in Climate, 5, https://doi.org/10.3389/fclim.2023.1158244, 2023.

Weatherford, C. L. and Gray, W. M.: Typhoon Structure as Revealed by Aircraft Reconnaissance. Part II: Structural Variability, Monthly Weather Review, 116, 1044–1056, https://doi.org/10.1175/1520-0493(1988)116<1044:TSARBA>2.0.CO;2, 1988.

Wei, M., Fang, G., Zhao, L., Wang, Z., Wang, J., Cao, S., and Ge, Y.: Comparative Study of Typhoon Wind Hazard Estimation in Coastal Region of China Using Different Wind Field Parameter Models, Journal of Wind Engineering and Industrial Aerodynamics, 236, 105 398, https://doi.org/10.1016/j.jweia.2023.105398, 2023.

Willoughby, H. E. and Rahn, M. E.: Parametric Representation of the Primary Hurricane Vortex. Part I: Observations and Evaluation of the Holland (1980) Model, Monthly Weather Review, 132, 3033–3048, https://doi.org/10.1175/MWR2831.1, 2004.

Xu, Z., Guo, J., Zhang, G., Ye, Y., Zhao, H., and Chen, H.: Global Tropical Cyclone Size and Intensity Reconstruction Dataset for 1959–2022 Based on IBTrACS and ERA5 Data, Earth System Science Data, 16, 5753–5766, https://doi.org/10.5194/essd-16-5753-2024, 2024.

Yasui, H., Ohkuma, T., Marukawa, H., and Katagiri, J.: Study on Evaluation Time in Typhoon Simulation Based on Monte Carlo Method, Journal of Wind Engineering and Industrial Aerodynamics, 90, 1529–1540, https://doi.org/10.1016/S0167-6105(02)00268-4, 2002.

## Appendix A: Surface Correction Parameter Calibration

The geostrophic drag law as shown in Equation 3, and the logarithmic wind profile, as shown in Equation 4, both require a surface parameter, $z_0$, to scale the gradient wind speed speed which is the output of the Holland model. The gradient wind speed is first scaled 10 m for comparison with IBTrACS, and subsequently to 100 m for the estimation of $U_{50}$. While $z_0$ is conventionally interpreted as the roughness length, this appendix explains why a strictly physical interpretation is possibly not appropriate here, and documents the reasoning behind the calibration of this parameter. This appendix also contains a brief discussion of the quality of the resulting fit.

A physically motivated approach to estimating $z_0$, aligning with a standard approach, is to apply the Charnock relation at each grid point and time step for each tropical cyclone as shown by the following equation:

$$z_0 = \alpha \frac{u_*}{g} \tag{A1}$$

where $z_0$ is the roughness length, $\alpha$ is the Charnock parameter, $u_*$ is the friction velocity and $g$ is gravity. To take this approach, $u_*$ is needed and can be derived from the gradient wind speed, however, $z_0$ is also present in this gradient wind speed formulation. To resolve the interdependence, the gradient wind speed formulation and Charnock relation were iterated over until consistent values are found and $z_0$ was also bound to a minimum of $7e^{-5}$ m (value described in Ott (2006)) and a maximum of $2e^{-4}$ m (accepted open ocean value) which are more physically reasonable values.

The resulting 10 m Holland model wind speeds were compared against the IBTrACS 10 m maximum wind speeds. The comparison revealed a systematic underestimation of the Holland 10 m wind speeds, with the distribution of percentage differences centred at approximately $-10\%$. Using this approach, distinct $u_*$ and $z_0$ can be calculated for each grid point, at each time step for each cyclone. However, a deficit of this magnitude is incompatible with the aims of this study.

This analysis relies on annual maxima to fit the Gumbel distribution, the maximum wind speed at any given time step is the quantity most likely to be selected for inclusion in the extreme value analysis, and errors in reproducing it propagate directly into the final $U_{50}$ estimate. A systematic underestimation in the calibration wind speed would produce correspondingly underestimated return levels, which is less than ideal.

Given the limitations of the Charnock approach, $z_0$ is instead treated as an empirical surface correction parameter. It is used as a scalar that maps gradient-level Holland model winds to the 10 m level which on average aligns with IBTrACS observations. This reinterpretation is justified by examining the Holland model. The Holland model is an empirical parametric model, so the analysis already operates outside a purely physical representation of TC wind structure.

Calibration is performed by identifying the value of $z_0$ for each region that minimises the mean percentage difference between the scaled Holland model 10 m wind speed and the IBTrACS 10 m maximum wind speed across all available data points. The surface correction parameters identified are $5 \times 10^{-6}$ m, $9 \times 10^{-6}$ m, and $1 \times 10^{-5}$ m for the Taiwan, Japan, and ECUS regions, respectively.

A key constraint on this calibration is that IBTrACS provides only the maximum wind speed at each time step; no spatial wind field is available. Calibration can therefore only be performed at the location of the maximum wind speed. Extending the calibrated $z_0$ spatially through additional assumptions would introduce further unquantifiable uncertainty, and is not pursued here.

$z_0$ is a non-varying value between times steps or TCs. This route was pursued because fitting the parameter to time steps or individual events would risk absorbing errors originating from both the Holland model and IBTrACS into the parameter itself, and could produce unstable values. A single, spatially uniform and temporally constant value is therefore adopted for each region. This ensures that variability in the $U_{50}$ results is driven by the statistics of the storm population rather than by the tuning of the surface parameter. The standard deviation of the residuals from the calibration fit is used as the uncertainty estimate for the scaled wind speed within the Monte Carlo analysis as shown in Table 9.

Figure A1 presents the probability density distributions of the differences between the scaled 10 m Holland wind speed and the IBTrACS 10 m values, calculated by the following equation:

$$\Delta u = 100 \times \left( \frac{u_{\mathrm{Holland}} - u_{\mathrm{IBTrACS}}}{u_{\mathrm{IBTrACS}}} \right) \tag{A2}$$

In all regions, 98.8% or more of the Holland model 10 m maximum wind speeds fall within $\pm 10\%$ of the corresponding IBTrACS value. This level of agreement is best understood in relation to the observational uncertainty inherent in IBTrACS itself. As documented in the IBTrACS technical documentation (IBTrACS Science Team, 2025) and summarised in Table 5, wind speed uncertainties since the year 2000 are approximately ±7 kt in the Northern Atlantic and ±10 kt in the Western Pacific. For category 5 storms, these correspond to approximately $\pm 5\%$ and $\pm 7\%$ respectively for category 1 storms these correspond to $\pm 9\%$ and $\pm 12\%$ respectively, closely aligning with the error when scaling the gradient Holland model wind speeds.

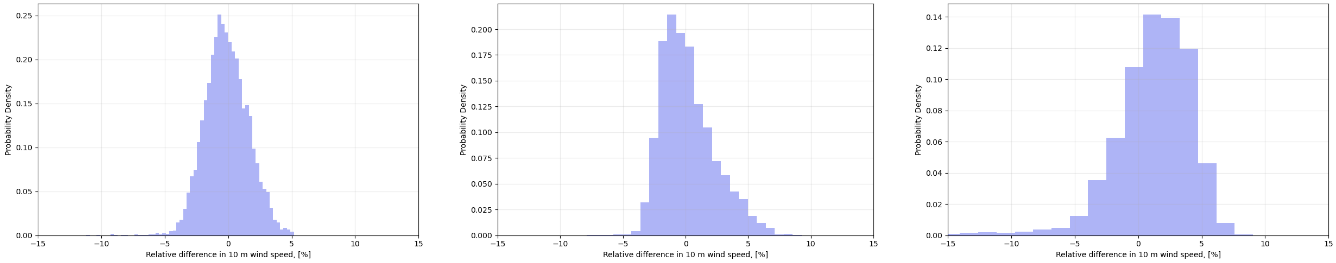

(a) (b) (c)

**Figure A1.** Comparison of maximum 10 m wind speeds from the Holland model and IBTrACS. The panels show the probability density distributions of the percentage difference, $\Delta u$, for (a) Taiwan, (b) Japan, and (c) ECUS.

A further feature of the distributions in Figure A1 is that they are not all perfectly symmetric about zero in all regions. Within the Taiwan region, the results look mostly symmetrical with 45.3% of values falling above 0. Within the Japan region, slight skew appears to the right, however, 46.6% of values fall above 0. Lastly, within the ECUS region the distribution skews to the left and 71% of data points are above 0. This means that the Holland model scaled wind speeds tend to exceed the IBTrACS reference, however this is a favourable outcome. A marginal positive bias in the calibration wind speed propagates to slightly elevated annual maxima and, consequently, slightly elevated $U_{50}$ estimates. Conservatism is likely desirable in the context of offshore infrastructure assessment.

## Appendix B: Abbreviations

| Abbreviation | Full Name |
|---|---|
| CFSR | Climate Forecast System Reanalysis |
| CMA | China Meteorological Administration |
| ECUS | East Coast of the United States |
| ERA5 | European Centre for Medium-Range Weather Forecast Reanalysis v5 |
| IBTrACS | International Best Track Archive for Climate Stewardship |
| IEC | International Electrotechnical Commission |
| JMA | Japan Meteorological Agency |
| HKO | Hong Kong Observatory |
| MERRA 2 | Modern-Era Retrospective analysis for Research and Applications |
| NOAA | National Oceanic and Atmospheric Administration |
| RMW | Radius of Maximum Winds |
| TC | Tropical Cyclone |
| US | United States |

*Author contributions.* KCS and XGL planned the study, KCS developed the method with input from XGL and MLB. KCS wrote the manuscript draft, and XGL and MLB reviewed and edited the manuscript.

*Competing interests.* No competing interests are present.

*Acknowledgements.* This project is funded by the European Union Horizon Europe MSCA Doctoral Network (HORIZON-MSCA-2022-DN-01-01, grant no. 101119550). The authors acknowledge the IBTrACS data availability (DOI: 10.1175/2009BAMS2755.1). We thank

Jana Fischereit and Niels Morten from DTU for their support. We further thank Søren Ott from DTU for his help and discussions. AI tools have been used to partially aid the writing of code to process the data and the formulation of some sentences within this paper.